A Bio-Inspired Event-Driven Mechanoluminescent Visuotactile Sensor for Intelligent Interactions

Kit-Wa Sou, Wang-Sing Chan, Kai-Chong Lei, Zihan Wang,* Shoujie Li, Dengfeng Peng,* and Wenbo Ding*

Event-driven sensors are essential for real-time applications, yet the integration of current technologies faces limitations such as high cost, complex signal processing, and vulnerability to noise. This work introduces a bio-inspired mechanoluminescence visuotactile sensor that enables standard frame-based cameras to perform event-driven sensing by emitting light only under mechanical stress, effectively acting as an event trigger. Drawing inspiration from the biomechanics of canine teeth, the sensor utilizes a rod-patterned array to enhance mechanoluminescent signal sensitivity and expand the contact surface area. In addition, a machine learning-enabled algorithm is designed to accurately analyze the interaction-triggered mechanoluminescence signal in real-time. The sensor is integrated into a quadruped robot's mouth interface, demonstrating enhanced interactive capabilities. The system successfully classifies eight interactive activities with an average accuracy of 92.68%. Comprehensive tests validate the sensor's efficacy in capturing dynamic tactile signals and broadening the application scope of robots in interaction with the environment.

1. Introduction

Tactile sensors are fundamental components in robotics and human–machine interfaces, enabling machines to perceive and respond to physical interactions with their environment. Unlike visual or auditory sensors, tactile sensors provide detailed information about pressure distribution, force, and contact points, making them essential for tasks like object manipulation, navigation, and providing haptic feedback. Traditional tactile sensors, including piezoresistive, capacitive, and optical waveguide types (Table S1, Supporting Information),[1] have limitations including response time, adaptability issues, and data redundancy due to continuous sampling regardless of tactile stimulus changes (Table S2, Supporting Information). Visuotactile sensors, such as GelSight,[2] aim to overcome these issues by combining visual and tactile sensing, using RGB LEDs and frame-based cameras to capture high-resolution surface deformations on the target rubber. However, the use of LEDs faces challenges such as thermal degradation and optical distortions,[3] along with data redundancy from frame-based cameras, persist.

To address these issues, integrating dynamic vision sensors (DVS) technology with visuotactile sensors has been explored.[4] Event-driven sensors, like DVS,[5] excel in applications requiring fast responses due to their ability to capture data only during significant changes, reducing redundancy and preserving essential information. These sensors mimic the biological retina, enhancing digital analysis of brightness shifts.[6] By adopting the event-driven approach, visuotactile sensors capture data only during significant tactile events, reducing redundancy while enhancing responsiveness. This integration improves temporal resolution and latency in dynamic tactile applications.

Despite these advancements, current DVS tactile sensors still face challenges in high costs, complex processing,[7] difficulty in capturing slowly varying signals,[8] and susceptibility to noise.[9] These limitations hinder their practicality and widespread adoption, underscoring the need for innovative solutions that maintain the advantages of event-driven sensing while addressing these issues.

A promising solution to these challenges is mechanoluminescence (ML), where select materials emit light under mechanical stress, directly converting physical pressure into luminescence, empowering frame-based cameras with event-driven visual sensing functions. The direct mechanical-to-optical conversion mechanism of ML materials eliminates the need for

K.-W. Sou, W.-S. Chan, K.-C. Lei, Z. Wang, S. Li, W. Ding
Shenzhen International Graduate School
Tsinghua University
Shenzhen 518055, P. R. China
E-mail: zihan.wang@berkeley.edu; ding.wenbo@sz.tsinghua.edu.cn
Z. Wang
Department of Mechanical Engineering
University of California
Berkeley, CA 94709, USA
D. Peng
Shenzhen Key Laboratory of Intelligent Optical Measurement and Detection
Key Laboratory of Optoelectronic Devices and Systems of Ministry of Education and Guangdong Province
College of Physics and Optoelectronic Engineering
Shenzhen University
Shenzhen 518060, P. R. China
E-mail: pengdengfeng@szu.edu.cn
W. Ding
RISC-V International Open Source Laboratory
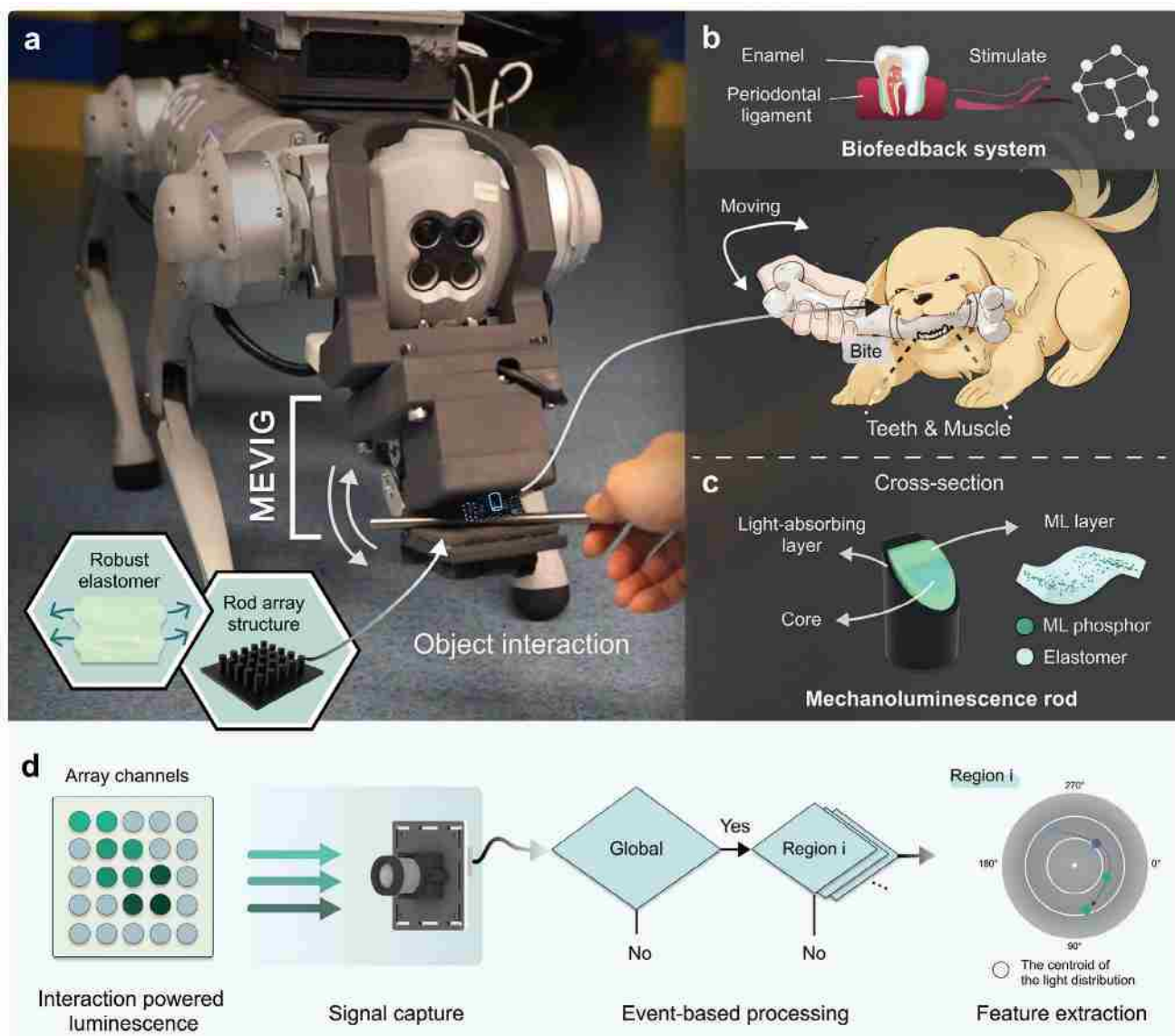Shenzhen 518055, P. R. China

2420872 (1 of 12)

Figure 1. Bio-inspired event-driven ML visuotactile sensor for intelligent interactions. a) Robot equipped with MAVIG as a mouth interface on a quadruped robot as mouth interface, highlighting the robust ML elastomer and rod array structure for object interaction. b) Schematic representation of a canine's biting mechanism, illustrating the dynamic interaction of teeth and muscles. c) Schematic of the ML rod showing stress concentration and cross-section with the light-absorbing layer, core, and ML layer. d) Diagram of the sensing and processing mechanism. Interaction-induced luminescence of ML sensor is captured by a camera from array channels and then processes signals using an event-driven method to identify tactile events globally and regionally. Feature extraction quantifies the ML emissions' intensity, as well as the radial distance and direction from the centroid.

electronic sensing elements at the contact interface, simplifying the sensor design while reducing susceptibility to environmental interference.[10] Recent bio-inspired advances include real-time mechanosensors and self-healing luminescent systems, demonstrating ML's potential in nature-inspired designs.[11] ZnS:Cu stands out for its self-recoverable emissions without the need for pre-excitation, providing stability and requiring lower activation pressure.[12] This material is integrated into flexible matrices like polydimethylsiloxane (PDMS), contributing to the development of durable, efficient sensors that operate independently of external power sources.[13] Moreover, the capabilities of ML materials can be enhanced, improving their luminescence properties and

self-recoverability, making them ideal for robust and stretchable devices.[14] These advancements facilitate the creation of wearable ML devices that enhance safety and offer new methods for stress monitoring.[15] Nevertheless, challenges such as ambient light interference and substrate durability remain, highlighting the need for ongoing research to optimize these materials for use in various industries.

In this study, we developed a bio-inspired mechanoluminescent visuotactile sensor that integrates a rod-patterned array embedded with mechanoluminescent phosphors within a flexible elastomer matrix (**Figure** 1a). The sensor enables standard frame-based cameras to perform low-cost, event-driven tactile

**ADVANCED
SCIENCE NEWS**

www.advancedsciencenews.com

**ADVANCED
FUNCTIONAL
MATERIALS**

www.afm-journal.de

sensing by emitting light only under mechanical stress, eliminating the need for external light sources. Inspired by the biomechanics of canine bites, this design incorporates a gripping mechanism that mimics the natural actions of a dog engaging its teeth, translating into a manipulation mechanism that captures pressure variations akin to natural touch (Figure 1b). Analogous to the way canine teeth utilize their hard enamel layers to efficiently transmit forces to the mechanoreceptors within the periodontal ligament, the rod structure directs stress toward the ML layer, thereby enhancing both force detection sensitivity and directional sensing capabilities.[16] (Figure 1c). An integrated light-absorbing layer ensures efficient operation in diverse lighting conditions. An ML-event-based processing method analyzes the emitted light under dynamic stimulation, measuring ML emission intensity, radial distance, and centroid direction to map applied forces across the sensor array (Figure 1d). The system achieves an average classification accuracy of 92.68% in distinguishing eight distinct interaction types. By integrating this sensor into a biomimetic mouth interface for quadruped robots, we developed the mechanoluminescent autonomous visuotactile interactive gripper (MAVIG), enabling the robot to interact with objects and respond to human directives swiftly. This advancement in mechanoluminescent materials and event-driven sensing mechanisms holds promise for enhancing tactile sensing capabilities in robotic systems, potentially leading to more intuitive and responsive human–machine interactions.

2. Results and Discussion

2.1. Biomimetic Mechanoluminescent Sensing Mechanism

The ML elastomer exhibits both unstretched and stretched states, illustrating how mechanical stress triggers light emission—the key to converting mechanical stimuli into optical signals (**Figure 2a**). Mimicking the dental structure of a dog, the patterned ML elastomer not only increases the contact area with objects compared to a flat surface, thus improving grip functionality as a mouth interface but also serves as a protective buffer, preventing damage when handling soft objects (Figure 2b).

The sensing module utilizes a patterned ML elastomer, operating on the principle of visuotactile sensing, which captures the ML layer (photon emitter) with a camera (photon receiver) in a structure optimized for capture angle and resilience to ambient light. We fabricated this patterned elastomer by doping it with ML particles, thereby reducing the need for complex wiring and minimizing energy consumption compared to conventional visuotactile sensors (Note S1, Supporting Information). The design integrates inorganic ML phosphors with organic elastomers, incorporating rod-shaped arrays that enhance sensing capabilities by facilitating the transmission of forces along each column.[17] However, a key challenge is selecting durable materials for the rods, as fragile blends are prone to breakage, which could compromise sensor functionality.

To overcome this challenge, we focused on enhancing efficiency and performance by optimizing the ML elastomer, thereby addressing the inherent limitations associated with the brittle nature of PDMS. The materials considered included Sorta-clear 37 (SC37), PDMS, Sorta-clear 10 (SC10), DragonSkin 30 (DS30), and Ecoflex 30 (EF30). The diversity in mechanical behavior reflects the varying polymer chain structures and cross-linking densities, impacting their ability to dissipate energy and, consequently, their ML performance.[18] Hence, it is crucial to balance ML sensitivity and durability during the selection. A series of images demonstrate the stress–strain characteristics of PDMS and SC37, revealing SC37's superior mechanical robustness (Figure 2c). The stress–strain curves of the materials with 30 weight percent (wt%) ZnS:Cu tested are presented (Figure 2d). These results illustrate differences in mechanical properties, such as tensile strength and elongation at break, attributed to variations in polymer chain structures and cross-linking densities. These differences in mechanical behavior are attributed to variations in polymer chain structures and cross-linking densities, which influence both mechanical energy dissipation and ML emission efficiency.[19] PDMS exhibited a tensile strength of up to 19.4 MPa but a relatively low elongation at less than 63.1% strain. In contrast, Ecoflex showed an exceptional elongation exceeding 534%, though its tensile strength was lower at only 5.4 MPa. SC37 displayed the highest tensile strength at 23.9 MPa with an elongation of 193%. Additionally, SC37's load–displacement curve (Figure S1, Supporting Information) indicates high strength and moderate elasticity. The steep initial slope suggests efficient energy transfer, crucial for ML intensity.

Simultaneously, the ML spectra (Figure 2e) display the intensities and spectral distribution of the candidate substrates when under mechanical strain, providing insights into their energy conversion efficiencies. For this instance, the composite films were doped with ZnS:Cu of 50 wt%. PDMS and SC37 exhibited superior peak intensities at 512 nm, indicating enhanced ML effects ideal for visibility and signal clarity. While PDMS demonstrated the highest Young's Modulus and peak intensity, its low strain capacity of 63% limited its applicability. In contrast, SC37 emerged as the optimal substrate for advanced ML stress sensing, offering the highest tensile strength, second-highest peak intensity (71.7% of PDMS's maximum), and a substantial elongation capacity of 196%. These results position SC37 as the prime candidate for the substrate of the ML sensor for advanced ML stress sensing.

Based on the selected substrate, an in-depth investigation was conducted about the impact of ZnS:Cu wt% content on the durability and ML efficiency of the composite film (Figure 2f,g). First, the impact on ML efficiency was studied. The composite film samples were fabricated with SC37 incorporated with ZnS:Cu, gradually increasing from 20% to 60%. The peak intensities increase with the additive content from 20 to 40 wt%. Once the content of ZnS:Cu particles reaches 50 wt%, the luminosity increases substantially, reaching a maximum value at 60 wt%. The intensity ratios reveal 60 wt% as the reference (100%), with 50 wt% at 62.24%, 40 wt% at 21.67%, 30 wt% at 17.83%, and 20 wt% at 5.13%. These results suggest that increased ZnS:Cu content leads to higher peak intensities. Further investigation of the 60 wt% demonstrates a linear relationship between applied force (0–16 N) and light emission intensity (Figure 2h), with an R^2 value of 0.97, which is in high agreement with previous reports.[20] This result again confirms the feasibility of using SC37 for precise force-sensing applications. SC37 was selected as the substrate for the ML sensor because of its superior mechanical properties and luminosity.
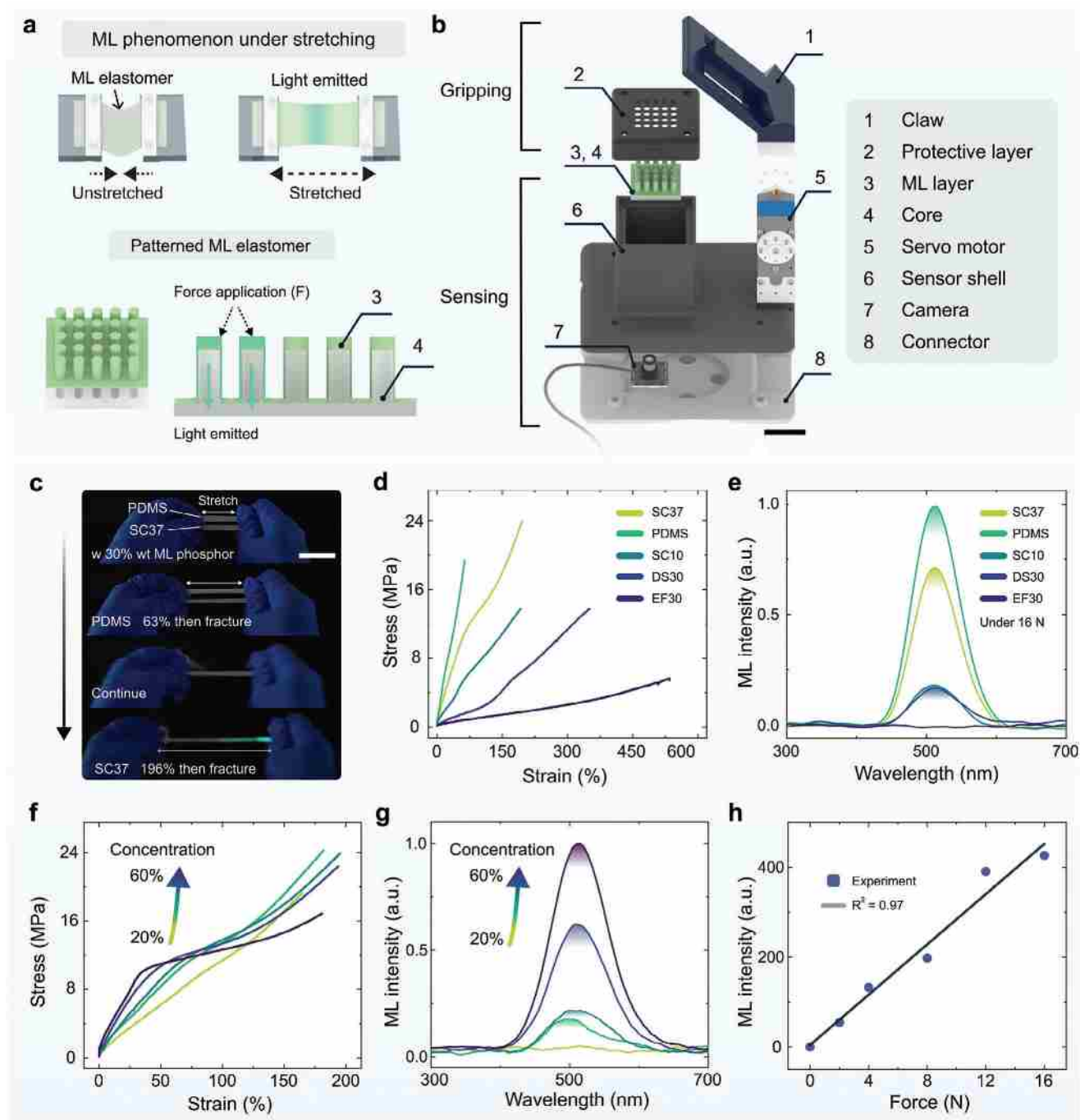
Figure 2. Design and material optimization. a) Schematic of the ML phenomenon: unstretched versus stretched states of ML elastomer. b) Diagram of the patterned ML elastomer of a 5 × 5 array structure emitting light to the bottom under mechanical forces. c) Sequence images for comparing the stretchability of PDMS and SC37 elastomers with 30 wt% ZnS:Cu ML phosphor. Scale bar, 4 cm. d) Stress–strain curves for various elastomers (SC37, PDMS, SC10, DS30, and EF30). e) ML intensity spectra for the elastomers under equal force. f) Stress–strain curve of varying doping concentrations in SC37 elastomer. g) Effect of different doping concentrations on luminous intensity. h) Force sensitivity of SC37 with 50 wt% phosphor. a.u., arbitrary units.
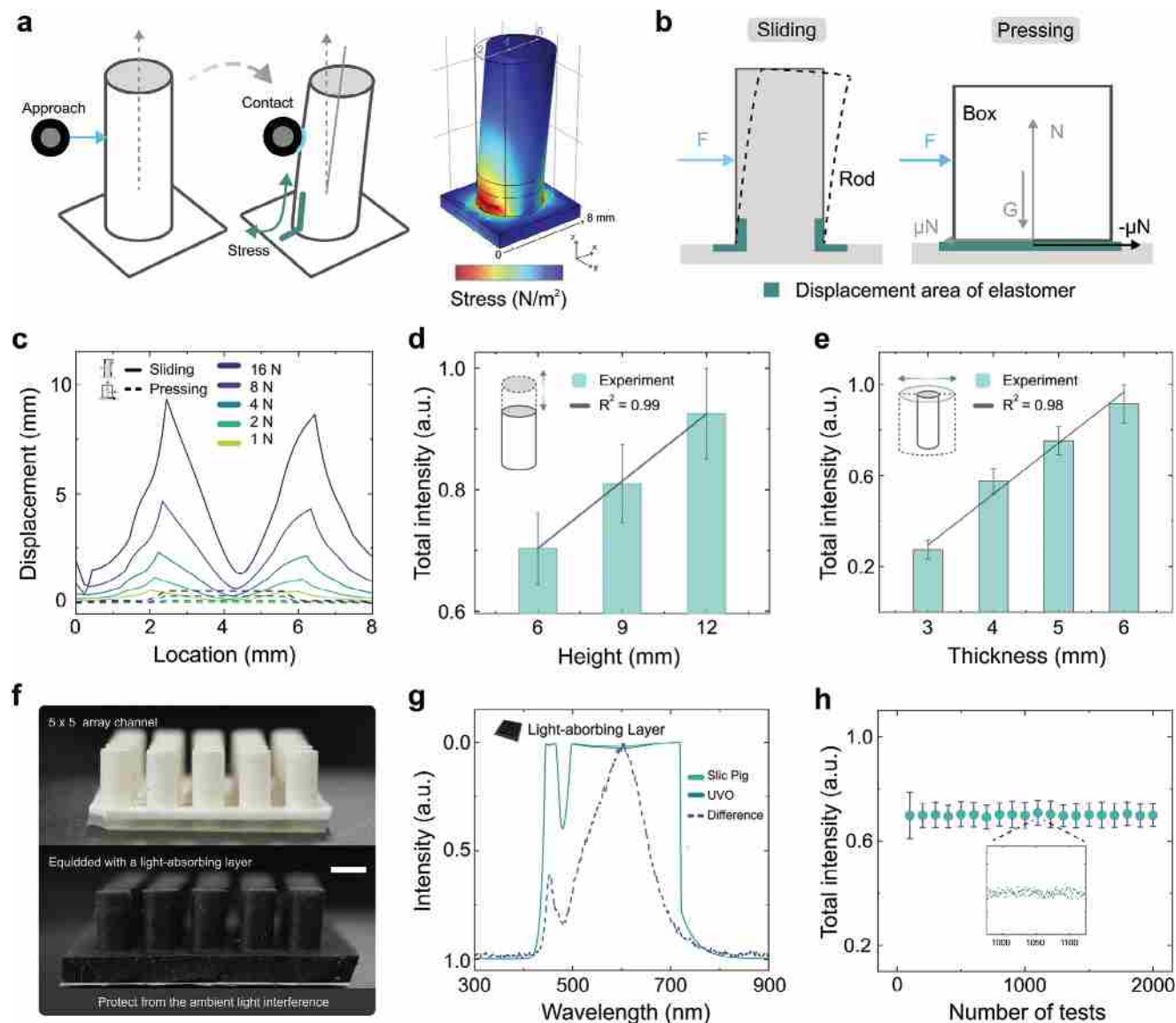
**ADVANCED
SCIENCE NEWS**

www.advancedsciencenews.com

**ADVANCED
FUNCTIONAL
MATERIALS**

www.afm-journal.de

Figure 3. Improving ML efficiency via structural optimization and simulations. a) Schematic illustration of the contraction mechanism and stress distribution in the ML elastomer during object interaction. b) Schematic contrasting a lateral sliding force on a single rod, resulting in shear deformation, with a combined vertical pressing and subsequent horizontal sliding force on a plane, detailing the respective displacement areas. c) Displacement profiles for varying forces (1–16 N) of figure b, illustrating the material's deformation response. d) Total ML intensity of the ML elastomer with heights ranging from 6–12 mm. e) Total ML intensity of the ML elastomer with rod diameters ranging from 3–6 mm. f) Image of 5 × 5 array channel of ML elastomers: the top image shows the array without a light-absorbing layer, while the bottom image shows the array with a light-absorbing layer. Scale bar, 5 mm. g) Spectral intensity comparison between two types of light-absorbing thin film. h) Stability test showing the total ML intensity over 2000 cycles of integrated ML sensor. Points represent mean values, and error bar represents SD for 100 test samples.

2.2. Improving ML Sensitivity via Structural Simulations and Optimization

We further investigate the structural refinement of the ML elastomer, which incorporates a cylindrical rod-patterned architecture inspired by the biomechanics of canines' bites (**Figure** 3a; Movie S1, Supporting Information). This biomimetic design is inspired by the stress localization observed in canine interactions with objects. In natural canine interactions, stress is strategically localized in areas like the enamel and periodontal ligament,

which are both adept at handling and transmitting mechanical forces. This process involves the transmission of stress from the enamel to the highly sensitive periodontal ligament, which is rich in nociceptors and mechanoreceptors that detect pressure.[21] By replicating this pattern, the ML elastomers are structured to concentrate stress at key points. Computational simulations of this design under lateral forces reveal significant stress concentrations at the rod bases, highlighted in warm colors on the heatmap to indicate areas of maximum ML activation potential. This confirms the design's effectiveness in force transduction.

Additionally, whereas a cylindrical object pressed against a rigid surface typically contacts along a single line, our compliant, rod-patterned design increases contact to multiple lines across each rod, further enhanced by the pressure exerted during clamping (Figure S2, Supporting Information). The structural elasticity substantially increases contact points, thus expanding the contact surface area and enhancing grip stability, allowing the material to wrap around and grasp objects more effectively.

To assess the impact of rod structural changes on ML sensitivity, the mechanical response of situation-specific elastomers to lateral forces is analyzed (Figure 3b). This comparison highlights the contrasting deformations: a lateral sliding force against a single rod resulting in localized shear deformation and a combined pressing and sliding force on a planar surface demonstrating distributed deformation. Finite-element analysis was performed to simulate these force applications (Figure 3c; Note S2, Supporting Information). The displacement analysis spans the x-coordinate (referred to as the "location") along the base from 0 to 8 mm, with the rod (8 mm in height, 4 mm in diameter) positioned between 2 and 6 mm. Results showed that displacement from sliding is significantly higher than from pressing under the same force levels. At higher forces, such as 16 N, displacement sharply peaks, highlighting the material's increased sensitivity to sliding. Elastomers in a rod array structure experience an average displacement 21.84 times greater under sliding than pressing on a flat surface, lowering the ML activation threshold. The sliding-to-pressing displacement ratio varied with applied force, ranging from 29.73 at 1 N to 16.94 at 16 N (Figure S3, Supporting Information), illustrating the changing sensitivity with force magnitude.

Further analysis of cylindrical rods' geometric dimensions reveals their influence on ML intensity. The emission levels, studied across rod heights from 6 to 12 mm at 3 mm intervals (Figures 3d and S4a, Supporting Information), showed a linear increase in luminescence with height; the shortest at 3 mm emitted an intensity of 0.7, while the tallest at 12 mm reached 1.0. However, 12 mm rods exhibited a higher tendency to fracture under stress compared to 9 mm rods. Considering this and the spatial constraints of the application as quadruped robots' mouth interface, the optimal rod height was set at 9 mm. Additionally, we investigated the effect of thickness on the rod from 3 to 6 mm. The result shows an increase in rod thickness correlated with higher luminescence (Figures 3e and S4b, Supporting Information). This increase can be attributed to the larger surface area available for ML emission despite the theoretical decrease in stress concentration. The sensitivity of the rod, which is a function of the induced strain per unit force, depends on the rod's geometric dimensions and material properties, as discussed in the Experimental Section. However, larger diameters reduced inter-rod spacing, potentially limiting individual rod movement. Considering the 36 mm sensor width of the quadruped robot, a 5 mm rod diameter was deemed optimal, enabling a 5 × 5 rod array configuration that optimizes ML intensity and structural integrity within this spatial constraint. This arrangement, covering a 36 × 36 mm² area, maximizes resolution and utilizes the available sensing surface efficiently.

To enhance the clarity and accuracy of ML visuotactile sensor readings under varied lighting conditions, a light-absorbing layer was added (Figures 3f and S5, Supporting Information). This design effectively shields the photon generation process from ex-ternal light influences, ensuring that only photons from the ML effect are captured by the sensor's camera, thus maintaining the robustness and functionality of the sensor. A comparative spectral analysis of Silc pig silicone pigments and UVO colorant was performed under indoor daylight lamps (50 W, 1.5 m above), confirming exceptional light absorption capabilities for both materials (Figures 3g and S6, Supporting Information). They block 99.9% of light across the spectrum from 400 to 850 nm, with Silc pig providing enhanced protection in the 492 to 577 nm range, crucial for protecting the green luminescence of the ZnS:Cu ML effect. This strategic inclusion of materials minimizes ambient light interference. These settings were integrated into the ML sensor design, and a repeatability test was conducted (Figure 3h). The test showed that the difference in luminous intensity was with an average of 6.92% under dynamic mechanical loads over 2000 cycles spanning 3 h and 20 min, verifying its durability. This integration of optimized material composition and bio-inspired structural design enables several fundamental advantages in our sensor design. The inherent event-driven sensing capability is achieved through direct mechanical-to-optical conversion, effectively eliminating continuous power consumption in operation. The rod-patterned structure enhances ML emission efficiency through optimized stress transfer pathways, while the tri-layer architecture provides robust operation under ambient lighting conditions. These design features work synergistically to create a sensor system that combines high sensitivity with operational stability and energy efficiency.

2.3. Signal Processing via Dynamic Luminescent Localization Mapper

We designed a specialized algorithm, dynamic luminescent localization mapper (DLLM), leveraging ML's property of emitting light only under dynamic mechanical stimulation, taking advantage of its stable dark background. Unlike conventional visuotactile sensors requiring internal LED illumination, the ML visuotactile sensor only needs to observe the unique phenomenon of the ML array in the dark interior. When there is no interaction, the camera records a dark scene and refrains from further processing, akin to the absence of events in a DVS system. During the interaction, light signals from each rod converge to a corresponding circular area at the elastomer's base, identified by the rod number. Similar to visuotactile sensing systems that consider marker points as taxels,[22] each circular area in the ML array functions as a visuotactile sensor taxel. However, unlike traditional visuotactile sensing systems, where taxels rely on displacement for tactile perception, each rod in the ML array corresponds to a fixed circular area in the frame. This fixed correspondence simplifies tracking and reduces computational requirements.

DLLM processes mechanical actions to compute and compare total and local ML intensities against preset thresholds (**Figure 4a**). If the total intensity exceeds this threshold, the algorithm further analyzes each region's intensity. Regions surpassing local thresholds are evaluated for the centroid of light distribution to identify interaction locations, while regions below the threshold are discarded. DLLM enhances precision and robustness by integrating spatial and temporal data. It utilizes a mathematical approach where the total luminance $H_n(t)$ of each
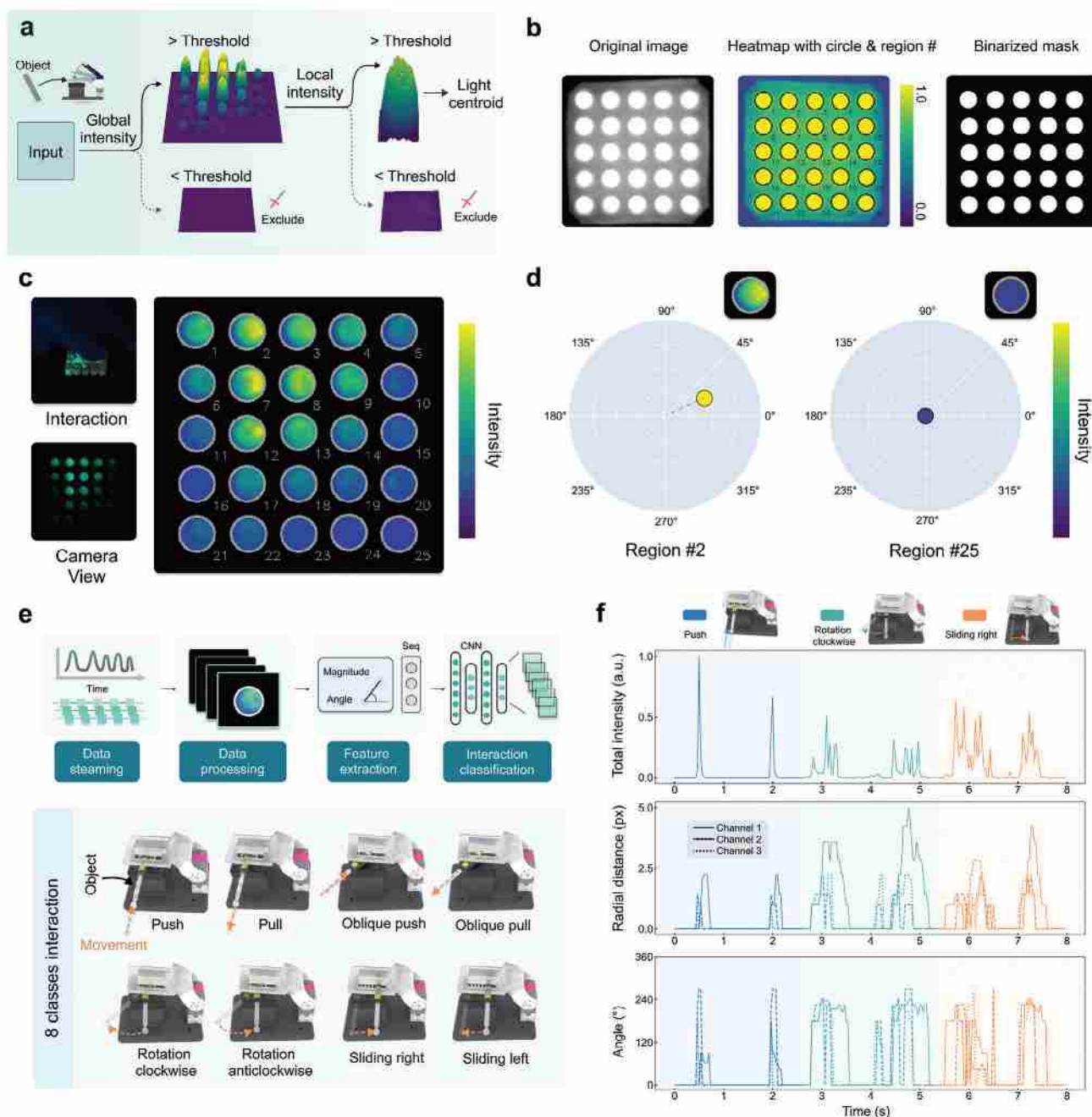
Figure 4. Proposed algorithm and interaction classification. a) Schematic of the dynamic luminescent localization mapper (DLLM) for ML visuotactile sensor. Input data from object interactions are processed to compute total intensity. Regions where intensity surpasses a predefined threshold are identified, and further analysis is performed to compute the centroid of the light distribution within these regions. b) Calibration and region mapping. c) Visualization of interaction intensity across a rod array. The camera view captures the interaction, which is then represented in a heatmap to show the intensity distribution. Higher intensity values indicate stronger interactions. d) Region gradient heatmap of interaction intensity, the radial distance, and the direction of the centroid of the ML distribution for two specific regions (#2 and #25) within the array. e) Interaction classification workflow. One of eight predefined actions' data is captured after the DLLM detects an effective frame. Features are extracted from each taxel and fed into the CNN algorithm for classification. f) Time series data for three different actions (blue line: push action, green line: clockwise rotation, orange line: sliding right action) in the time domain. Different channels (Channels 1–3) are compared to highlight interaction patterns.

**ADVANCED
SCIENCE NEWS**

www.advancedsciencenews.com

**ADVANCED
FUNCTIONAL
MATERIALS**

www.afm-journal.de

taxel A_n is calculated using a double integral that accounts for the spatial distribution of light intensity across the sensor area. This method allows for precise assessment of changes, enhancing detection accuracy. The algorithm employs a dual-threshold system to minimize false positives and ensure reliable change detection. Global and local thresholds $\alpha \times D$ (where α is the scaling factor and D is the global average frame intensity) and $\beta \times B_n$ (where β is the local scaling factor and B_n is the average intensity for each taxel's circular area), respectively, are used to filter out minor or irrelevant changes effectively. Such thresholds provide stability by maintaining consistent output amidst fluctuating data inputs. Additionally, the system's recovery from disruptions is expedited by its real-time processing capability and continuous adjustment of thresholds based on recent data inputs, ensuring rapid recalibration and resumption of normal operations. For calibration, a lamp is positioned above the ML sensing array, capturing a frame which is then converted to grayscale (Figure 4b). Image noise is minimized via Gaussian blur, and then the Hough circle algorithm identifies and organizes circular outlines by their centers and radii, creating a binarized mask. This mask stores the hardware calibration parameters, which remain valid in unchanged settings. Upon activation, the sensor uses these parameters to accurately locate taxel areas.

During operation, if the total intensity of a frame does not satisfy the global event-driven threshold, the frame is discarded. This is analogous to DVS's ability to ignore scenes with minimal overall change, reducing data processing. Additionally, if the intensity of any circular area meets the local event-driven threshold, the frame is considered effectively triggered (Figure 4c). All effective frames undergo further feature extraction, starting with calculating the weighted centroid coordinates for each circular area. Based on the center coordinates and weighted centroids, an offset vector is calculated and converted into polar coordinates, recording the vector's length and polar angle as the radial distance and direction of the centroid of the ML distribution (Figure 4d). Systematic testing demonstrates robust directional force detection with an average angular measurement error of ±3.41° within 0° to 90° range (Figure S7, Supporting Information). The radial symmetry of our rod-patterned architecture enables the extension of this sensing capability to the complete 360° range. Along with the total intensity of the circular area, these parameters serve as the feature values of the rod, characterizing its sensory data. Detailed descriptions of DLLM are provided in Note S3 and demonstrated in Movie S2, Supporting Information.

The calibration and operational efficacy of DLLM validate the effectiveness of the ML visuotactile sensor as MAVIG in real-world applications (Figure 4e). The system initiates with an interaction, such as a gripper holding an object, and streams dynamic stress distribution data. Key features like the radial distance and direction of the centroid of the ML distribution are extracted and classified using a convolutional neural network (CNN). A practical demonstration involved using a screwdriver, with training data from ten individuals performing eight distinct actions, resulting in 100 samples per action and a training-to-testing ratio of 8:2 (Note S4, Supporting Information). This setup highlights the system's ability to accurately interpret human inputs and its adaptability in interactive applications. Further analysis of three actions—"Push," "Rotation clockwise," and "Sliding right"—using time-series data emphasizes the system's sensitiv-

ity and precision (Figure 4f). Each action's ML intensity and angle were evaluated across two consecutive samples. The first row aggregates intensity data from 25 channels, with "Push" showing the highest intensity due to direct force. Subsequent rows depict the magnitude and angle for specific channels, illustrating stress diversity and direction. For example, "Push" shows a brief consistent angle, while "Sliding right" maintains a constant angle longer. These variations offer detailed physical interpretations, enriching the dataset and improving the machine learning model's predictive accuracy and adaptability to different physical interactions in real-world applications.

Following the detailed analysis of individual actions, the MAVIG system aggregates radial distance and angle of the centroid of the ML distribution data from all 25 channels into 50 time-series datasets, which are then processed by a CNN to classify the actions observed (Figure S8, Supporting Information). This combination of data types is selected based on its demonstrated efficacy in enhancing action recognition, effectively capturing the spatial diversity and directional nuances necessary for accurate classification. The performance is substantiated through validation tests, which show that the system achieves an average classification accuracy of 92.68% with a validation loss of 27.53% (Figure S9, Supporting Information).

2.4. Integration as an Intelligent Mouth Interface

The MAVIG system was integrated as a mouth interface on a quadruped robot to enhance its environmental interactions. Such an interface reduces mechanical complexity and weight compared to alternatives like a third arm, thus enhancing balance, energy efficiency, and spatial efficiency in confined spaces (Note S5, Supporting Information). The hardware incorporates a smaller servo motor and the sensor shell to enhance the system's robustness and functionality (**Figure 5a**). By rapidly processing tactile inputs, the robot can perform tasks such as following a designated path when guided by touch, manipulating objects, and responding to human commands delivered through specific interaction patterns. For instance, when a user slides an object across the mouth interface in a certain direction, the robot interprets this as a command to move forward or turn, enabling intuitive control without external devices and contributing to improved performance in interactive tasks.

We developed an interactive movement system, as outlined in the flowchart (Figure 5b), that enables the robot to perceive and respond to its environment autonomously. The ML visuotactile sensing unit, comprising a camera and ML sensor, captures detailed sensory information during physical interactions. This sensory data is transmitted to the processor, which houses the controller that manages the robot's actions, such as moving forward, backward, and rotating. The DLLM processes the sensory data rapidly to identify ML tactile features. The interaction recognition unit then classifies these features into interaction categories, which determine motion commands. These commands are executed by the quadruped robot, enabling it to further interact with the environment.

A specialized task demonstrates the robot navigating a designated track under human guidance through this interactive system (Figure 5c; Movie S3, Supporting Information). In this
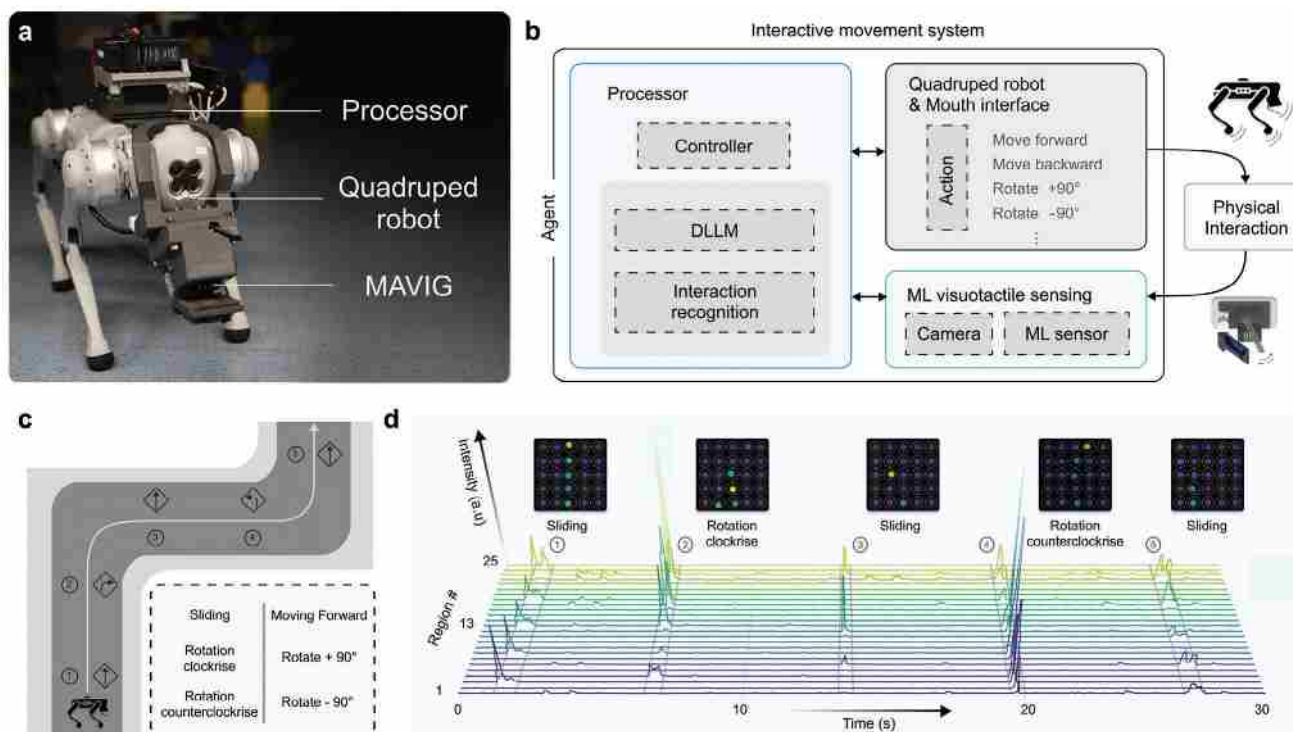
Figure 5. Integration of the MAVIG into a quadruped robot as a mouth interface for interactive movement demonstration. a) Photograph of a quadruped robot equipped with the MAVIG mouth interface, showcasing the processor and mouth interface for interaction capabilities. b) Schematic of the interactive movement system. c) The path of navigation task using the interactive movement system. d) Time-series diagram displays the responses to external interactions captured by the MAVIG system. The plot shows ML intensity over time across different regions of the sensor array, highlighting detected interactions in inlets, including sliding and rotations (clockwise and counterclockwise). These responses are processed and classified into interaction types, triggering the corresponding movement commands to the quadruped robot.

task, the robot successfully followed tactile cues provided by the user through the mouth interface, showcasing its ability to navigate complex environments based on touch interactions. The processor analyzed the event-driven signal using DLLM and a pre-trained CNN, which simplifies the classification system from eight to four categories to enhance computational efficiency and accuracy, achieving an overall accuracy of 97.37%. Validation tests revealed that the mouth interface had a response time of less than 0.7 s. The time-series visualization of ML responses effectively correlates external interactions with the MAVIG system (Figure 5d), showcasing the interactive movement system allows the robot to explore and respond to physical interactions autonomously.

3. Conclusion

We have developed an event-driven ML visuotactile sensor utilizing rod-pattern SC37 elastomers embedded with ZnS:Cu, chosen for its superior luminescent efficiency and mechanical robustness. By adopting ML for visuotactile sensing, we replaced RGB LEDs, effectively addressing issues related to power consumption, thermal degradation, and optical distortions. We designed a rod-patterned architecture inspired by the biomechanics of canine bites to optimize tactile sensitivity and enhance interaction capabilities.

Filtering techniques eliminate ambient light sensitivity, ensuring consistent sensor performance across various lighting conditions. The integration of the DLLM further refines the processing flow, enhancing feature extraction and system efficacy in real-world applications. This method empowers traditional cameras with event-driven sensing, avoiding the high costs and complexity of DVS.

The ML visuotactile sensor system, demonstrated here as part of the mouth interface for quadruped robots, significantly enhances these robots' environmental interaction capabilities. Although the system is calibrated for quadruped robots, adaptations can be made to suit scenarios with atypical designs or specific functional requirements. The robust nature of these ML sensors not only prolongs their useful life but also augments the system's energy efficiency, promoting a sustainable approach. Notwithstanding the remaining limitations and future work, demonstrating the effectiveness of ML visuotactile sensors compared with traditional RGB LED-based systems represents a milestone in tactile sensing and robotics.

Future research will aim to refine these integrations and extend their applications, potentially broadening the scope of sensory interfaces. This includes developing irregularly shaped or arranged ML rods to accommodate diverse interaction patterns. It is hoped that continued innovation in ML sensor technology and algorithm optimization will lead to more nuanced and effective interactions.

4. Experimental Section

Material and Characterization: Among the various ML materials reported,[23] the most notable include asymmetric piezoelectric compounds such as strontium aluminate ($SrAl_2O_4:Eu^{2+}$) and $ZnS:Cu/Mn^{2+}$.[24] Strontium aluminate required pre-irradiation to activate ML,[25] while $ZnS:Cu/Mn^{2+}$ exhibited self-recoverable emissions without the need for pre-excitation, providing stability and requiring lower activation pressure.[12] This property rendered $ZnS:Cu/Mn^{2+}$ suitable for this application, and ZnS:Cu recorded a high durability and brightness.[12a]

Mechanical stimulation of ZnS:Cu particles induced plastic deformation, resulting in the bending of energy bands within the material's electronic structure. This deformation facilitated the quantum tunneling of electrons from shallow donor states to the conduction band. The subsequent recombination of these excited electrons with holes in the valence band led to the emission of photons in the green and blue spectral regions. This ML process effectively transduced mechanical energy into visible light, demonstrating the intricate relationship between structural perturbations and electronic transitions in doped semiconductor materials.[26]

ML phosphors ZnS:Cu were purchased from Shanghai Keyan Optoelectronics Technology. The phosphor size (about an average of 30 μm) and morphology were characterized using a scanning electron microscope (Hitachi, SU8010) (Figure S8a,b, Supporting Information). X-ray powder diffraction was performed using an X-ray powder diffractometer (D8 Advance) (Figure S10c–e, Supporting Information). For the elastomer, PDMS (Dowsil 140) was acquired from Dow Corning. Sorta-clear 37 (SC37), Sorta-clear 10 (SC10), DragonSkin30 (DS30), and Ecoflex 30 (EF30), as well as Silc pig silicone color pigment, were purchased from Smooth-on Inc.

Preparation of Material Performance Evaluation: To prepare the polymer matrices, a 10:1 mass ratio of PDMS precursor and curing agent was combined in a vessel. Concurrently, ZnS:Cu ML phosphors were mixed with PDMS at a 1:1 ratio using a Planetary Centrifugal Mixer (THINKY MIXER ARE-310) at 2000 rpm for 90 s at ambient temperature. This procedure was repeated for four silicone elastomer types: SC37, SC10, DS30, and EF30, each mixing with a 1:1 mass ratio of parts A and B. Following mixing, the blend was degassed under vacuum for 10 min to eliminate air bubbles. The blend was then cast into molds tailored for specific tests. For the sample for tension testing, the homogenized phosphor-elastomer blend was then cast onto an ISO37 Type 1 stand mold. The fabrication process for this system is documented (Figure S11, Supporting Information). The resulting elastomer was thermally cured at 60 °C for 1 h and allowed to cool to room temperature. Additionally, elastomers with varied phosphor concentrations were prepared to investigate the effects of differing elastomer substrates on the mechanical properties. For the sample for ML Measurement, the blend was evenly distributed onto a plastic sheet using a scraper to ensure uniform thickness and similarly cured. The resulting film was thermally cured at 60 °C for 1 h and allowed to cool to room temperature. This process yielded ML films with thicknesses of ≈300 μm. Additionally, films with varied phosphor concentrations were prepared to investigate the effects of differing elastomer substrates on the mechanoluminescent properties.

Tension Testing of ML Elastomer: ML elastomers were prepared into a dumbbell shape (135 mm × 25 mm) with a test length of 25 mm, which is in accordance with the ISO37 Type 1 stand mold requirement. The stress–strain curves of the ML elastomer samples were retrieved using the universal testing machine (micro-force tensiometer, Instron, Microtester 5948).

Luminous Intensity Measurements of ML Film: The ML films were placed between two ends of a fixer of a Prtronic FT2000 Flexible Electronics Tester (Shanghai Mifang Electronic Technology Co., Ltd) (Figure S12, Supporting Information). The stretching was generated with one of the ends shifting forward and backward 30 mm repeatedly on a rail at a speed of 40 mm s^{-1}. ML was collected via an optical fiber and transmitted to a spectrometer (Ocean Optics QE65 Pro) for recording. The spectrometer integration time was set to 2.0 s.

Preparation of Rod Array ML Sensor: The fabrication process for this system is documented (Figure S13, Supporting Information). During the fabrication of a 5 × 5 rod array ML sensor, elastomer molding was exploited. The mold consists of five 3D-printed parts: the internal fork and filters, the external fork and filters, and a base mold. The spacing between rods was critically designed to accommodate the elastic deformation at the rod base during lateral force application, ensuring reliable mechanical response and ML signal generation. The external fork and filter shaped the external layer with spaces for the middle layer. Similarly, the internal counterparts allow room for the core layer, shaping the elastomer into rod form. The construction of the ML sensor included the following: First, the light-absorbing layer (composed of SC37 with 2 wt% Silc pig black pigment) was transferred onto the base mold and vacuumed at 30 kPa to remove bubbles. The external fork was placed onto the mold, initiating the external layer's inner structure, with the filter securing the fork. Upon solidification, the external fork and filter were detached from the base mold while keeping the light-absorbing layer in its position. The ML layer was then poured on top of the external layer and vacuumed. The internal fork and filter shaped the ML layer and were removed after hardening. Subsequently, the core layer was added, with existing slots providing shape. Following the solidification of the core layer, the 5 × 5 rod array ML sensor was demolded and ready for system integration.

Force Sensitivity of the ML Rod: This model analyzed the deformation of the ML rod under lateral force and the resultant strain at its base. When a lateral force F is applied to the tip of a rod with a fixed base, it creates a bending moment $M = F \times L$ at the base. The rod's cross-section has a moment of inertia $I = \pi r^4/4$, where r is the radius. The maximum bending stress at the surface ($y = r$) is given by

$$\sigma_{max} = \frac{4FL}{\pi r^3} \tag{1}$$

this stress induces an axial strain which is given by

$$\epsilon_{max} = \frac{\sigma_{max}}{E} = \frac{4FL}{\pi r^3 E} \tag{2}$$

where E is the Young's modulus.

The sensitivity S of the rod, defined as the strain per unit force, is

$$S = \frac{d\epsilon}{dF} = \frac{4L}{\pi r^3 E} \tag{3}$$

Optimization of ML Rod Dimensions: A UR5 robotic arm with a custom 3D printed probe (Tip has a contact area of 5 cm^2) was attached at the terminal. The test sample of an ML sensor was secured onto the testbed (Movie S2, Supporting Information), performing just the basic sensing elements. It contained a cover, acrylic glass, an ML sensor, a sensor shell, and a camera. A light-blocking cloth covered the setup to prevent external light interference, ensuring the reliability of ML data under controlled lighting conditions. The chosen camera component was the DeHong IMX415, a 30 frames per second (FPS) color CMOS. The frame rate of the detector was set to 30 FPS, and the later chosen camera remained the same. The arm swiped over the ML rods, moving at a constant speed of 200 mm s^{-1} (Figure S14, Supporting Information), triggering ML emissions by varying the rods' diameter and height to optimize sensor responses.

Light-Absorbing Ability Test: Silc pig silicone pigments and UVO colorant were each incorporated at 2 wt% into SC37 to create a thin film of ≈300 μm thickness. The mixture was processed in a spin machine and then subjected to a light test using indoor daylight lamps (50 W, 1.5 m above the sample). Light spectra were captured using an optical fiber and analyzed with a spectrometer (Ocean Optics QE65 Pro), which had an integration time set at 2.0 s. The performance difference is defined as

$$\frac{I_x - I_{Silc\ Pig}}{I_{Silc\ Pig}} \times 100\%, \tag{4}$$

where I_x is the spectral intensity of the comparison material under evaluation, and $I_{Silc Pig}$ is the spectral intensity of Silc pig.

Repeatability Test: With the UR5 robot moving at a constant speed of 200 mm s^{-1}, the probe repeatedly swiped the ML sensor with a light-absorbing layer. The ML elastomer sample was measured for 2000 cycles, 6.0 s for one cycle, spanning 3 h and 20 min.

Assembly of MAVIG System: The MAVIG system's design includes a Gripper (elements 1–5) and a sensing module (elements 3–8) housed within a 170 mm × 120 mm × 120 mm unit with a 36 mm × 36 mm sensing surface (Figure S15, Supporting Information). The gripping system, featuring a protective layer and a claw, maximizes friction and accommodates various object shapes. The sensing module utilizes the principle of visuotactile sensing, which is achieved by capturing the ML layer (photon emitter) with a camera (photon receiver) within a structure that optimizes the capture angle and is resilient to ambient light. The ML sensor was secured between the protective layer and a plane acrylic lens, connected using shared M3 screw holes. For actuation, a 60 N m^{-1} torque digital servo motor (Hiwonder LD-260MG, 65 mm × 30 mm × 61 mm) was attached tightly to the sensor foundation. The 3D resin-printed claw features an inner flat soft layer (Compat 45, measuring 36 mm × 36 mm) that grips objects securely. Activation occurs through the rotation of the motor shaft, which presses the object between the claw's inner surface and the sensing layer, enabling effective trapping and sensing of the object's characteristics. Two types of connectors were used: one affixed to the base of the gripping system for attaching the MAVIG system to a robotic arm and another for attaching to a quadruped robot. The chosen camera component was DeHong IMX415, which was set to a frame rate of 30 FPS in this work, ensuring adequate ML emission capture while maintaining real-time processing and preventing data transmission bottlenecks. Notably, the absence of an LED circuit in the design minimizes heat effects, allowing the MAVIG system to operate without temperature-related disruptions during extended use.

Prototype Applications: For the demonstration, the MAVIG system was integrated as a mouth interface on a quadruped robot (UnitreeRobotics, GO1) using a custom connector (Figure 5a). The robot's size was 645 mm × 280 mm × 400 mm. It was equipped with a processor (Intel NUC 12 Pro mini, i7 core, Iris Xe graphics, dimensions: 117 mm × 112 mm × 56 mm) and a dual-output power source (22 V, split into 19 V for the processor and 7 V for the digital servo motor). The processor connects to the quadruped robot and the MAVIG (the motor and camera) through USB 3.1. To optimize integration with the quadruped robot, the dimensions of MAVIG were adjusted by selecting a 35 N m^{-1} digital servo motor (DSSERVO, RDS3235, dimensions: 40 mm × 20 mm × 40 mm) and reducing the height of the sensor shell from 65 to 50 mm, ensuring a compact fit and enhanced functionality. The processor-processed data from MAVIG through DLLM can utilize pre-trained CNN to interpret interaction patterns for fast response. The process was implemented on the processor using Python. The classification system was streamlined from eight to four categories to optimize computational efficiency and accuracy. "Sliding right" and "Sliding left" were merged into "Sliding"; "Pull," "Push," "Oblique pull," and "Oblique push" were combined into "Push/Pull." The categories for "Rotation clockwise" and "Rotation anticlockwise" were maintained separately. The overall accuracy was 97.37% (Figure S18, Supporting Information). After recognizing interactions, the processor translates these into executable commands for the quadruped robot.

Interaction-Based Movement: Interaction patterns "Sliding," "Rotation clockwise," and "Rotation counterclockwise" corresponded to the forward, turning right, and turning left functions, respectively, and the interaction pattern "Push/Pull" controlled switching between biting and releasing. The quadruped robot control was achieved using the processor. During operation, interaction pattern data were first transmitted to the processor. After the data were classified and processed, the corresponding action command was sent to the robot. The time-series trajectories of the quadruped robot controlled by interaction with an object interaction from a person demonstrated the system's responsiveness to autonomy in navigating and exploring.

Supporting Information

Supporting Information is available from the Wiley Online Library or from the author.

Conflict of Interest

The authors declare no conflict of interest.

Author Contributions

K.-W.S., W.-S.C., and K.-C.L. designed the experiments, analyzed the data, and drafted the manuscript. K.-W.S. and W.-S.C. performed the characterization of the material. K.-W.S., W.-S.C., and K.-C.L. conducted the functional experiments for the ML sensor. K.-W.S. and K.-C.L. designed and implemented DLLM algorithm. W.-S.C. and K.-C.L. contributed to the mechanical design and assembly of the MAVIG system. K.-W.S., W.-S.C., S.L., and Z.W. designed the control systems and integrated the mouth interface of the quadruped robot. K.-W.S., W.-S.C., and Z.W. performed the related demonstrations. K.-W.S. conducted theoretical analysis and simulations. S.L., Z.W., D.P., and W.D. revised the manuscript. All authors discussed the results and provided comments on the manuscript.

Data Availability Statement

The data that support the findings of this study are available from the corresponding author upon reasonable request.

[1] a) Y. H. Jung, J.-Y. Yoo, A. Vázquez-Guardado, J.-H. Kim, J.-T. Kim, H. Luan, M. Park, J. Lim, H.-S. Shin, C.-J. Su, R. Schloen, J. Trueb, R. Avila, J.-K. Chang, D. S. Yang, Y. Park, H. Ryu, H.-J. Yoon, G. Lee,

H. Jeong, J. U. Kim, A. Akhtar, J. Cornman, T.-i. Kim, Y. Huang, J. A. Rogers, *Nat. Electron.* **2022**, *5*, 374; b) K. Yao, J. Zhou, Q. Huang, M. Wu, C. K. Yiu, J. Li, X. Huang, D. Li, J. Su, S. Hou, Y. Liu, Y. Huang, Z. Tian, J. Li, H. Li, R. Shi, B. Zhang, J. Zhu, T. H. Wong, H. Jia, Z. Gao, Y. Gao, Y. Zhou, W. Park, E. Song, M. Han, H. Zhang, J. Yu, L. Wang, W. J. Li, et al., *Nat. Mach. Intell.* **2022**, *4*, 893.

[2] W. Yuan, S. Dong, E. H. Adelson, *Sensors* **2017**, *17*, 2762.

[3] a) S. Wang, Y. She, B. Romero, E. Adelson, in *2021 IEEE Int. Conf. on Robotics and Automation (ICRA)*, IEEE, Piscataway, NJ **2021**, pp. 6468–6475; b) M. H. Tippur, E. H. Adelson, in *2023 IEEE Int. Conf. on Soft Robotics (RoboSoft)*, IEEE, Piscataway, NJ **2023**, pp. 1–8; c) M. Lambeta, P. W. Chou, S. Tian, B. Yang, B. Maloon, V. R. Most, D. Stroud, R. Santos, A. Byagowi, G. Kammerer, D. Jayaraman, R. Calandra, *IEEE Robot. Autom. Lett.* **2020**, *5*, 3838; d) J. Zhao, E. H. Adelson, in *2023 IEEE/RSJ Int. Conf. on Intelligent Robots and Systems (IROS)*, IEEE, Piscataway, NJ **2023**, pp. 8979–8984; e) Y. She, S. Q. Liu, P. Yu, E. Adelson, in *2020 IEEE Int. Conf. on Robotics and Automation (ICRA)*, IEEE, Piscataway, NJ **2020**, pp. 10075–10081; f) S. Q. Liu, E. H. Adelson, in *2022 IEEE Int. Conf. on Soft Robotics (RoboSoft)*, IEEE, Piscataway, NJ **2022**, pp. 925–931.

[4] a) B. Ward-Cherrier, N. Pestell, N. F. Lepora, *Presented at 2020 IEEE Int. Conf. on Robotics and Automation (ICRA)*, Piscataway, NJ, May **2020**; b) K. Kumagai, K. Shimonomura, *Presented at 2019 IEEE World Haptics Conf. (WHC)*, Piscataway, NJ, July **2019**.

[5] a) P. Lichtsteiner, T. Delbruck, in *2005 PhD Research in Microelectronics and Electronics*, IEEE, Piscataway, NJ, **2005**, pp. 202–205; b) C. Posch, T. Serrano-Gotarredona, B. Linares-Barranco, T. Delbruck, *Proc. IEEE* **2014**, *102*, 1470; c) G. Gallego, T. Delbrück, G. Orchard, C. Bartolozzi, B. Taba, A. Censi, S. Leutenegger, A. J. Davison, J. Conradt, K. Daniilidis, *IEEE Trans. Pattern Anal. Mach. Intell.* **2020**, *44*, 154.

[6] a) F. Zhou, Z. Zhou, J. Chen, T. H. Choy, J. Wang, N. Zhang, Z. Lin, S. Yu, J. Kang, H.-S. P. Wong, *Nat. Nanotechnol.* **2019**, *14*, 776; b) Z. Zhang, S. Wang, C. Liu, R. Xie, W. Hu, P. Zhou, *Nat. Nanotechnol.* **2022**, *17*, 27; c) A. Dodda, N. Trainor, J. M. Redwing, S. Das, *Nat. Commun.* **2022**, *13*, 3587; d) Y. Zhou, J. Fu, Z. Chen, F. Zhuge, Y. Wang, J. Yan, S. Ma, L. Xu, H. Yuan, M. Chan, *Nat. Electron.* **2023**, *6*, 870.

[7] a) D. Gehrig, A. Loquercio, K. G. Derpanis, D. Scaramuzza, *Proceedings of the IEEE/CVF Int. Conf. on Computer Vision*, IEEE, Piscataway, NJ **2019**, pp. 5633–5643; b) S. Tulyakov, D. Gehrig, S. Georgoulis, J. Erbach, M. Gehrig, Y. Li, D. Scaramuzza, *Proceedings of the IEEE/CVF Conf. on Computer Vision and Pattern Recognition*, IEEE, Piscataway, NJ **2021**, pp. 15155–16164.

[8] a) Z. Sun, N. Messikommer, D. Gehrig, D. Scaramuzza, *European Conf. on Computer Vision*, Springer Nature, Switzerland **2022**, pp. 341–357; b) E. Perot, P. De Tournemire, D. Nitti, J. Masci, A. Sironi, *Adv. Neural Inf. Proc. Syst.* **2020**, *33*, 16639.

[9] S. Ding, J. Chen, Y. Wang, Y. Kang, W. Song, J. Cheng, Y. Cao, *IEEE Trans. Multimedia* **2023**, *26*, 65.

[10] H. Bai, S. Li, J. Barreiros, Y. Tu, C. R. Pollock, R. F. Shepherd, *Science* **2020**, *370*, 848.

[11] a) B. Zhou, X. Yang, J. Liu, L. Lan, H. Lu, Y. Wang, Z. Wei, X. Zhang, *Nano Lett.* **2024**, *24*, 8198; b) X. Qiu, J. Liu, B. Zhou, X. Zhang, *Adv. Funct. Mater.* **2023**, *33*, 2300321.

[12] a) S. M. Jeong, S. Song, S.-K. Lee, B. Choi, *Appl. Phys. Lett.* **2013**, *102*, 051110; b) K.-S. Sohn, S. Timilsina, S. P. Singh, T. Choi, J. S. Kim, *APL Mater.* **2016**, *4*, 106102; c) V. K. Chandra, B. P. Chandra, P. Jha, *Appl. Phys. Lett.* **2013**, *103*, 161113.

[13] a) C. Wang, R. Ma, D. Peng, X. Liu, J. Li, B. Jin, A. Shan, Y. Fu, L. Dong, W. Gao, Z. L. Wang, C. Pan, *InfoMat* **2021**, *3*, 1272; b) N. Zhang, B. Tian, Z. Wang, A. T. Smith, Z. Ma, Z. Xue, L. Sun, *Adv. Opt. Mater.* **2021**, *9*, 2100137; c) F. Han, T. Wang, G. Liu, H. Liu, X. Xie, Z. Wei, J. Li, C. Jiang, Y. He, F. Xu, *Adv. Mater.* **2022**, *34*, 2109055; d) X. Qian, Z. Cai, M. Su, F. Li, W. Fang, Y. Li, X. Zhou, Q. Li, X. Feng, W. Li, X. Hu, X. Wang, C. Pan, Y. Song, *Adv. Mater.* **2018**, *30*, 1800291.

[14] a) C. Li, Q. He, Y. Wang, Z. Wang, Z. Wang, R. Annapooranan, M. I. Latz, S. Cai, *Nat. Commun.* **2022**, *13*, 3914; b) W. Wang, S. Wang, Y. Gu, J. Zhou, J. Zhang, *Nat. Commun.* **2024**, *15*, 2014. c) Z. Xie, Y. Xue, X. Zhang, J. Chen, Z. Lin, B. Liu, *Nat. Commun.* **2024**, *15*, 3668.

[15] a) Y. Zhuang, R.-J. Xie, *Adv. Mater.* **2021**, *33*, 2005925; b) J. Xiao, Y. Cai, Y. Song, H. Tang, P. Zhang, Q. Peng, X. Xu, Z. Liu, L. Zhao, *Laser Photonics Rev.* **2024**, *18*, 2301002; c) B. Tian, Z. Wang, A. T. Smith, Y. Bai, J. Li, N. Zhang, Z. Xue, L. Sun, *Nano Energy* **2021**, *83*, 105860; d) B. Hou, L. Yi, C. Li, H. Zhao, R. Zhang, B. Zhou, X. Liu, *Nat. Electron.* **2022**, *5*, 682; e) J. Zhang, B. Xu, K. Chen, Y. Li, G. Li, Z. Liu, *SusMat* **2024**, *4*, e207.

[16] a) W. K. Dong, T. Shiwaku, Y. Kawakami, E. H. Chudler, *J. Neurophysiol.* **1993**, 1567; b) M. Trulsson, R. S. Johansson, K. A. Olsson, *J. Physiol.* **1992**, *447*, 373; c) K. Choy, E.-K. Pae, Y. Park, K.-H. Kim, C. J. Burstone, *Am. J. Orthod. Dentofacial Orthop.* **2000**, *117*, 98.

[17] S. M. Jeong, S. Song, K.-I. Joo, J. Kim, S.-H. Hwang, J. Jeong, H. Kim, *Energy Environ. Sci.* **2014**, *7*, 3338.

[18] a) K. C. Galloway, Y. Chen, E. Templeton, B. Rife, I. S. Godage, E. J. Barth, *Soft Rob.* **2019**, *6*, 671; b) F. Yang, Y. Yuan, R. P. Sijbesma, Y. Chen, *Macromolecules* **2020**, *53*, 905.

[19] a) J. Gan, M. G. Kang, M. A. Meeker, G. A. Khodaparast, R. J. Bodnar, J. E. Mahaney, D. Maurya, S. Priya, *J. Mater. Chem. C* **2017**, *5*, 5387; b) P. Sotta, P.-A. Albouy, M. Abou Taha, B. Moreaux, C. Fayolle, *Polymers* **2021**, *14*, 9.

[20] M. V. Mukhina, J. Tresback, J. C. Ondry, A. Akey, A. P. Alivisatos, N. Kleckner, *ACS Nano* **2021**, *15*, 4115.

[21] a) R. Jacobs, D. van Steenberghe, *J. Periodontal Res.* **1994**, *29*, 153; b) T. Maeda, K. Ochi, K. Nakakura-Ohshima, S. Youn, S. Wakisaka, *Crit. Rev. Oral Biol. Med.* **1999**, *10*, 307.

[22] N. F. Lepora, *IEEE Sens. J.* **2021**, *21*, 21131.

[23] a) D. Peng, S. Qu, in *Functional Tactile Sensors* (Eds: Y. Zhou, H.-H. Chou), Elsevier, Amsterdam, Netherlands, **2021**, Ch. 6; b) Z. Huang, B. Chen, B. Ren, D. Tu, Z. Wang, C. Wang, Y. Zheng, X. Li, D. Wang, Z. Ren, S. Qu, Z. Chen, C. Xu, Y. Fu, D. Peng, *Adv. Sci.* **2023**, *10*, 2204925.

[24] a) T. Zhou, H. Chen, J. Guo, Y. Zhao, X. Du, Q. Zhang, W. Chen, T. Bian, Z. Zhang, J. Shen, W. Liu, Y. Zhang, Z. Wu, J. Hao, *Small* **2023**, *19*, 2207089; b) B. P. Chandra, V. K. Chandra, P. Jha, D. Pateria, R. N. Baghel, *Luminescence* **2016**, *31*, 67; c) N. Wang, M. Pu, Z. Ma, Y. Feng, Y. Guo, W. Guo, Y. Zheng, L. Zhang, Z. Wang, M. Feng, X. Li, D. Wang, *Nano Energy* **2021**, *90*, 106646; d) R. Sharma, U. Sharma, *J. Alloys Compd.* **2015**, *649*, 440.

[25] N. Terasaki, C.-N. Xu, *Jpn. J. Appl. Phys.* **2009**, *48*, 04C04C150.

[26] a) A. Qasem, P. Xiong, Z. Ma, M. Peng, Z. Yang, *Laser Photonics Rev.* **2021**, *15*, 2100276; b) V. Chandra, B. Chandra, P. Jha, *Appl. Phys. Lett.* **2013**, *103*, 161113; c) S. W. Shin, J. P. Oh, C. W. Hong, E. M. Kim, J. J. Woo, G.-S. Heo, J. H. Kim, *ACS Appl. Mater. Interfaces* **2016**, *8*, 1098.

ADVANCED FUNCTIONAL MATERIALS

Supporting Information

A Bio-Inspired Event-Driven Mechanoluminescent Visuotactile Sensor for Intelligent Interactions

Kit-Wa Sou, Wang-Sing Chan, Kai-Chong Lei, Zihan Wang*, Shoujie Li, Dengfeng Peng* and Wenbo Ding*

Supporting Information

A Bio-inspired Event-Driven Mechanoluminescence Visuotactile Sensor for Intelligent Quadruped Robot Interactions

Kit-Wa Sou[1,†], Wang-Sing Chan[1,†], Kai-Chong Lei[1,†], Zihan Wang[1,2*,], Shoujie Li[1,], Dengfeng Peng[3*,] Wenbo Ding[1,4*]

1. Shenzhen International Graduate School, Tsinghua University, Shenzhen 518055, China

2. Department of Mechanical Engineering, University of California, Berkeley 94709, USA

3. Shenzhen Key Laboratory of Intelligent Optical Measurementand Detection; Key Laboratory of Optoelectronic Devices and Systems of Ministry of Education and Guangdong Province, College of Physics and Optoelectronic Engineering, Shenzhen University, Shenzhen 518060, PR China

4. RISC-V International Open Source Laboratory, Shenzhen 518055, China

† These authors contributed equally: Kit-Wa Sou, Wang-Sing Chan, Kai-Chong Lei

*Corresponding author. Email: zihan.wang@berkeley.edu (Z. Wang)
pengdengfeng@szu.edu.cn (D. Peng) ding.wenbo@sz.tsinghua.edu.cn (W. Ding)

Notes

Note S1. Power consumption comparison of visuotactile sensors

To quantify the amount of power saved by incorporating the ML phosphors ZnS:Cu, we designed an experiment to investigate the power consumption of other visuotactile sensors. Consequently, we can compare the power consumption of different visuotactile sensors. The experiment utilizes a USB power meter (ZHAOXIN U65-B voltage and current tester), which is inserted in between a visuotactile sensor (connected to the receptacle of the USB power meter) and the computer (with the USB power meter plugged into the computer). Subsequently, the USB power meter measures the power being drawn from the connected sensor, with the sensor adjusted to its maximum capture resolution for consistency.

Our comparative analysis focused on the commercial DIGIT sensor, which represents conventional visuotactile sensor architecture. DIGIT requires multiple electrical components including RGB LED arrays (4-6 LEDs), LED driver circuits, and power distribution PCB, necessitating 12-18 distinct wiring points for operation. In contrast, our ML-based design eliminates these components entirely, requiring only USB connectivity for the camera module.

We compared the energy consumption of the commercial DIGIT sensor, which uses LEDs, with our ML-based sensing system (Figure S14). Replacing DIGIT's LEDs with ML phosphors and removing the LED management PCB could reduce its energy consumption from 1.222 W to just the camera's 120 mW, potentially saving 90.18% in energy. Additionally, our system, using a DeHong IMX415 camera module, consumes 0.542 W, substantiating a 55.65% energy reduction compared to DIGIT. These findings underscore the efficiency of ML phosphors in lowering power consumption in sensor technology.

Note S2. Simulation setting

The simulation involved a rod elastomer (Sliding) and a plane elastomer with a steel object above (Pressing), both modeled from PDMS, featuring Young's modulus of 550 kPa, a Poisson's ratio of 0.49, and a density of 970 kg m^{-3}. Each elastomer measured 10 mm × 10 mm × 2 mm with a fixed base. The rod had an additional cylindrical part, 8 mm in height and 4 mm in diameter. The plane elastomer was topped by a steel block sized 2 mm × 2 mm × 4 mm. Lateral forces were applied 2 mm above the contact surface on the rod and the steel block, simulating realistic cutting force application, with gravity considered in the calculations. Simulation software COMSOL Multiphysics 6.0 was exploited here. Although PDMS was chosen due to its well-characterized properties in the literature, experimental validation confirms that SC37 exhibits similar deformation patterns, with magnitude differences proportional to the differences in their Young's modulus.

Note S3. Workflow of DLLM

The initial phase of DLLM involves the process of calibration and threshold initialization. The calibration process includes several steps. Firstly, a 40W handheld white light LED lamp is placed above the ML sensor (Using an ML sensor of identical dimensions but lacking a light-absorbing layer), and a frame ($350 \times 350 \times 3$ pixels) is recorded from the sensor camera. This frame is converted to a grayscale image. Image noise is reduced, and detail levels are lowered through Gaussian blur processing. Then, using the Hough Circle algorithm, the center coordinates $c_n(x, y)$ and the corresponding radii r_n of each circular outline are pinpointed and sorted by the coordinates of the circle centers from smallest to largest. The center coordinates and the average radius are given by:

$$C = \{c_n(x, y)\}_{n=1,2,\ldots,25} \tag{1}$$

$$\bar{R} = \frac{\left(\sum_{k=1}^{n} r_k\right)}{n} \tag{2}$$

By using (1) and (2), a binarized mask is obtained, thus storing the hardware calibration parameters as $P = (C, \bar{R}) \in \mathbb{R}^{n+1}$. It is important to note that the hardware calibration parameters P remain valid as long as the ML sensor maintains its original size and is not disassembled. Once the ML sensor initiates, it only needs to load the hardware calibration parameters P to find the frame area A_n corresponding to each taxel. For threshold initialization, video frames from 1.0 s preceding the captured frames are used for initializing event-driven parameters. The global average intensity of the frame is given by:

$$D = \sum_{t=1}^{FPS} \frac{M(t)}{FPS} \tag{3}$$

Then it is calculated, where the total brightness of each frame $M(t)$ is given by:

$$M(t) = \sum_{x=1}^{350} \sum_{y=1}^{350} I(x, y) \tag{4}$$

Similarly, the average intensity for each circular area is calculated as a local threshold:

4

$$B_n = \sum_{t=1}^{FPS} \frac{H_n(t)}{FPS} \tag{5}$$

$H_n(t)$ denotes asthe total measurement of one of the circular areas and is given by:

$$H_n(t) = \iint_{A_n} I(x,y)dA = \sum_{\phi=0}^{2\pi} \sum_{\rho=0}^{R} I(c_{n,x} + \rho\cos(\phi), c_{n,y} + \rho\sin(\phi)) \tag{6}$$

During the operation, if the total intensity of a frame is not satisfied, $M(t) > \alpha D$ the frame is not saved or processed further, where α is the global event-driven threshold. In addition, if the total intensity of any circular area satisfies $H_n(t) > \beta B_n$, the frame is considered as an effectively triggered frame, where β is the local event-driven threshold. An example of an effectively captured frame triggered by DLLM (Figure 4c).

Conventional image processing methods typically require frame-wide analysis (350×350 pixels), necessitating 122,500 operations per frame regardless of event occurrence. This $O(WH)$ complexity, where W and H represent frame dimensions, introduces significant computational overhead and potential susceptibility to ambient noise. Our DLLM implementation employs a two-stage approach combining global thresholding ($M(t) > \alpha D$) with targeted regional processing ($N \times \pi r^2$), where $N = 25$ taxels and $r = 20$ pixels. This strategic reduction in processed pixels (from 122,500 to approximately 31,416 per frame) achieves a 74.4% improvement in computational efficiency while maintaining robust event detection capabilities.

All effective frames are subjected to further feature extraction. Starting with calculating the weighted centroid coordinates for each circular area:

$$q_n(t) = (q_{n,x}, q_{n,y}) = \left(\frac{\iint_{A_n} xI(x,y)dA}{\iint_{A_n} I(x,y)dA}, \frac{\iint_{A_n} yI(x,y)dA}{\iint_{A_n} I(x,y)dA} \right) = \left(\frac{U_{n,x}(t)}{H_n(t)}, \frac{U_{n,y}(t)}{H_n(t)} \right) \tag{7}$$

$$U_{n,x}(t) = \sum_{\phi=0}^{2\pi} \sum_{\rho=0}^{R} (c_{n,x} + \rho\cos(\phi))I(c_{n,x} + \rho\cos(\phi), c_{n,y} + \rho\sin(\phi)) \tag{8}$$

$$U_{n,y}(t) = \sum_{\phi=0}^{2\pi} \sum_{\rho=0}^{R} (c_{n,y} + \rho\sin(\phi))I(c_{n,x} + \rho\cos(\phi), c_{n,y} + \rho\sin(\phi)) \tag{9}$$

Based on the center coordinates and weighted centroids, an offset vector is calculated:

$$\vec{v}_n(t) = \left(v_{n,x}, v_{n,y}\right) = q_n(t) - c_n = \left(\frac{U_{n,x}(t)}{H_n(t)} - c_{n,x}, \frac{U_{n,y}(t)}{H_n(t)} - c_{n,y}\right) \qquad (10)$$

These vectors are then converted into polar coordinates, recording the vector's length $l_n(t)$ and polar angle $\omega_n(t)$. Together with the total intensity $H_n(t)$ of the circular area, serves as the feature values of the taxel $Z_n(t) = (H_n, l_n, \omega_n)$. These parameters together characterize the taxel's sensory data (Figure 4d). A pseudocode of DLLM is provided (Figure S15).

Note S4. Interaction identification performance evaluation

For the eight interactions classification, the MAVIG system was attached to the terminal of a UR5 robot arm via it's inherited attachment unit with M6 screws. A metal screw (M8, 7.7 mm × 160 mm) was selected as an interactive object. It was placed on the sensor, occupying 21% of the sensing area. The participants interact with the object held by MAVIG with a 5 × 5 rod patterned ML sensing layer. The processing with DLLM retained only radial distance and direction data of the ML distribution centroids. The time series data for the CNN is segmented into samples using a window size of 8. The dataset is divided, with 80% for training and 20% for model validation. The CNN model architecture starts with a Conv1D layer with 32 filters using the ReLU activation function; then, it goes through batch normalization and downsampling to arrive at another Conv1D layer with 128 filters. Subsequently, two dense layers with ReLU activation functions follow, followed by a final dense layer utilizing SoftMax as the activation function to output the classification probabilities. The model achieved a classification accuracy of 92.68% (Figure S9). The process was implemented in Python.

Note S5. Mouth interfaces vs. third arms

The study on quadruped robots mainly focuses on localization and mapping but lacks manipulation capabilities, limiting their usefulness in many applications.[S1] Enhancing these robots with robotic arms transforms them into mobile manipulators, allowing environmental interaction. However, adding an arm introduces challenges, including increased weight and payload constraints, which can impact the robot's balance and energy efficiency. Moreover, motion planning becomes complex. Some approaches treat the arm as an independent system, simplifying control but risking inaccessibility if the subsystems are poorly positioned.[S2] An integrated whole-body control approach offers optimal performance but requires sophisticated algorithms.[S3]

In contrast, equipping quadruped robots with a mouth interface instead of a third arm offers distinct advantages. Psychologically, a mouth interface resonates more with human users due to its familiarity, enhancing emotional connection, particularly in therapeutic or social robots.[S4] It maintains a balanced and streamlined design, reducing mechanical complexity and weight, which improves the robot's balance and energy efficiency—key factors for longevity and maneuverability. Additionally, integrating a mouth interface utilizes the robot's existing body plan more effectively, which is especially beneficial in confined spaces where a third arm hinders maneuverability and accessibility.
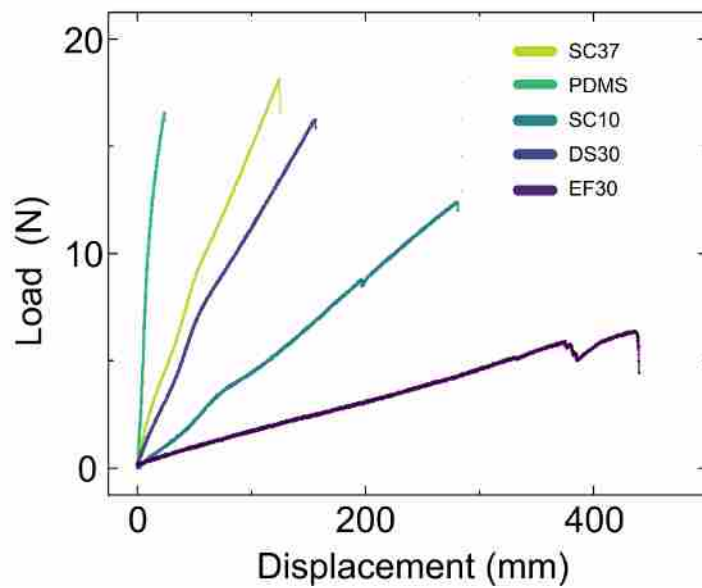
Figure S1. Load-displacement curve of the 5 substrate candidates: Sorta-clear 37 (SC37), Polydimethylsiloxane (PDMS), Sorta-clear 10 (SC10), DragonSkin30 (DS30), and Ecoflex 30 (EF30)
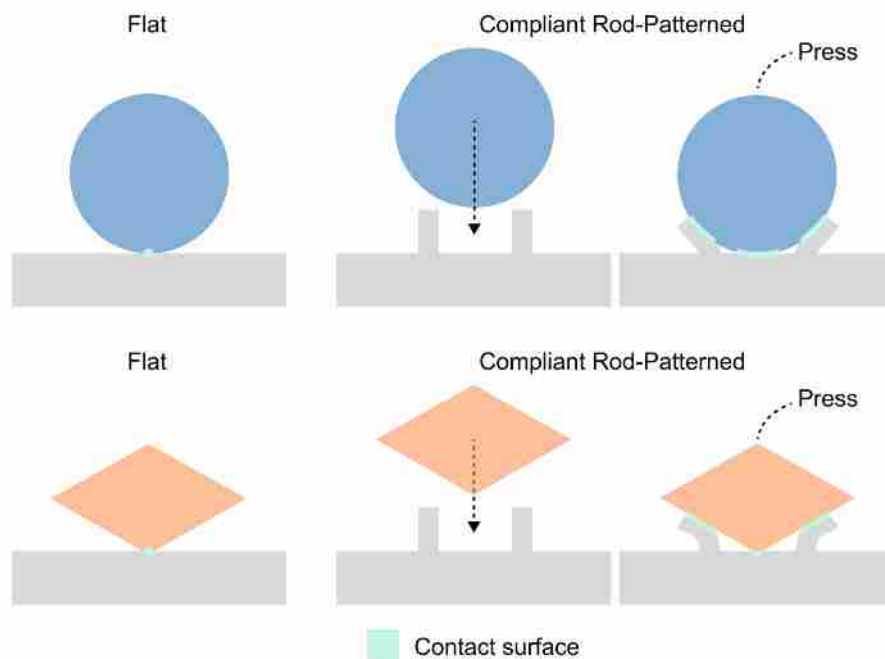
Figure S2. Schematic depiction of spherical and diamond-shaped objects engaging with a flat and a rod-patterned surface. An objects show single-point contact (green) with the flat surface; a counterparts adapt to the rod-patterned surface contours, depicted by increased contact surface, illustrating the importance of compliance in achieving multi-point contact.
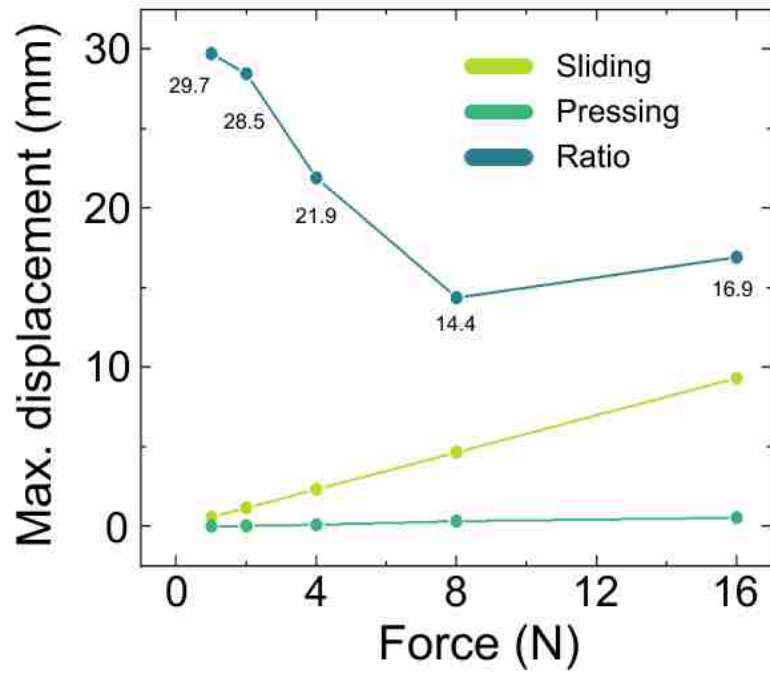
Figure S3. The graph illustrates the relationship between force and maximum displacement for Sliding and Pressing motions, as well as the ratio of Sliding to Pressing.
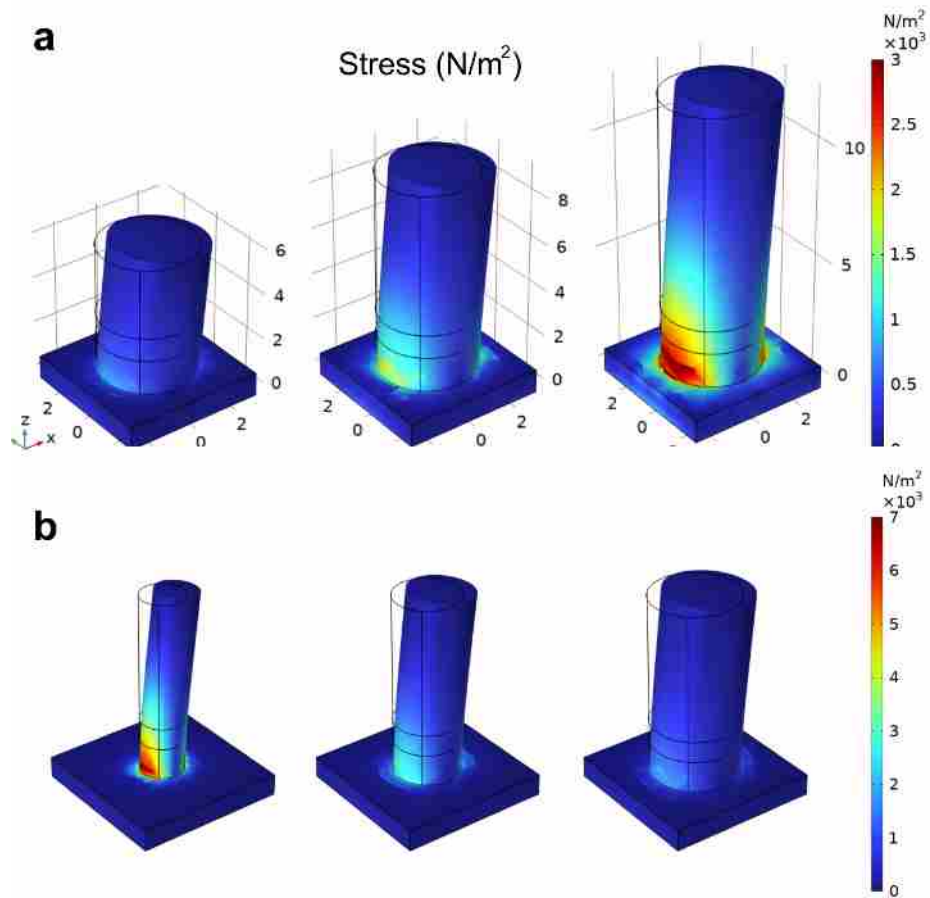
Figure S4. Stress Distribution in Cylindrical Structures with Variable Geometry. a) Cylinders of uniform radius and increasing height, revealing a consistent high-stress zone at the base across heights. **b)** Illustrates cylinders of uniform height with increasing radii, where a larger radius corresponds to a broader high-stress region at the base.
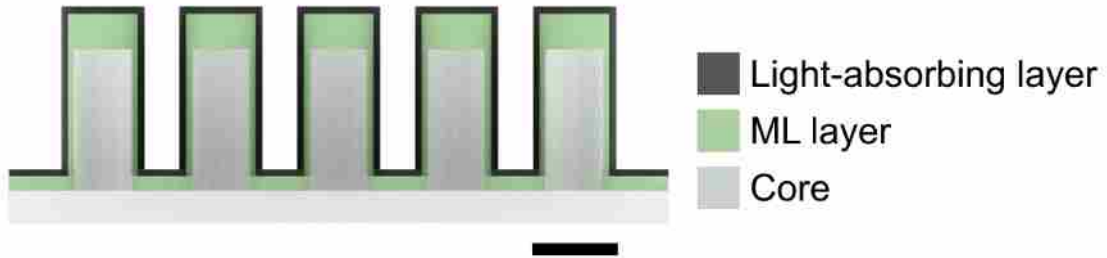
Figure S5. The design schematic of the tri-layered ML rod elastomer containing: the light-absorbing layer, ML layer and the core. Scale bar, 5 mm.
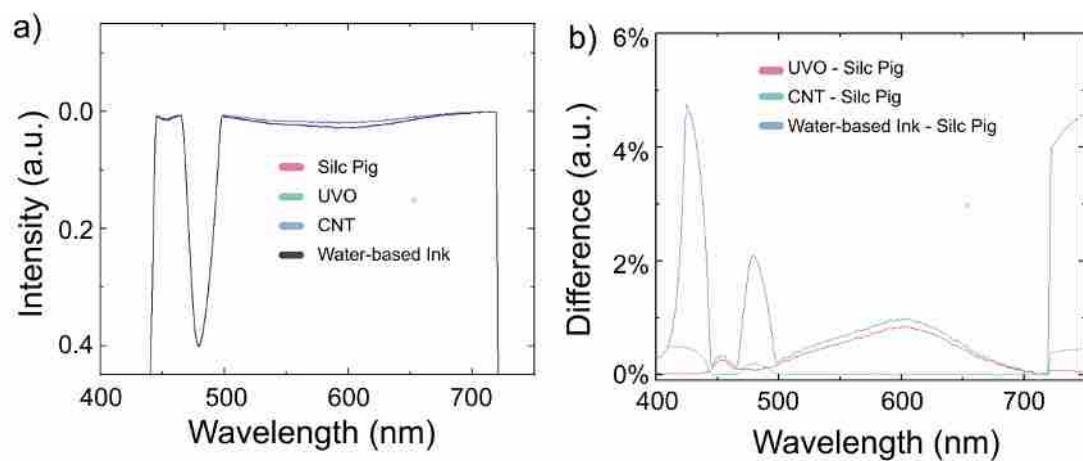
Figure S6. Comparative analysis of light-absorbing materials: Silc Pig, UVO, CNT, and Water-based Ink a) Spectral intensity comparison of four absorbing materials across wavelengths from 400 nm to 900 nm. b) Performance difference comparison between UVO and Silc Pig CNT and Silc Pig, and Water-based ink and Silc Pig across wavelengths from 400 nm to 900 nm.
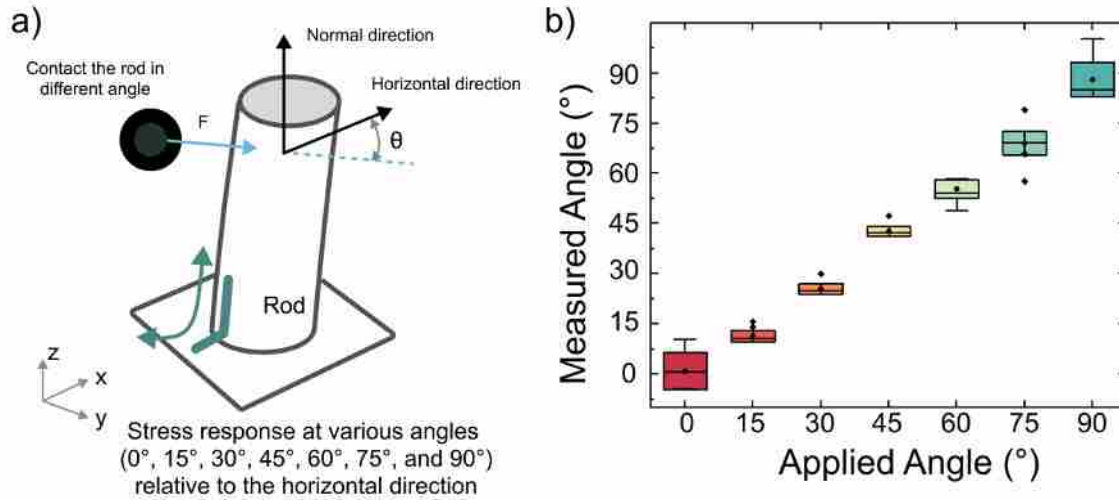
Figure S7. Experimental characterization of force direction sensitivity. a) Schematic illustration of the testing setup, showing the interaction between the sensor and a vertical cylindrical rod at various angles (θ) relative to the horizontal direction. Force (F) is applied by controlling the approach angle while maintaining constant movement speed. b) Box plot distribution of measured angles versus applied angles (0°, 15°, 30°, 45°, 60°, 75°, and 90°).
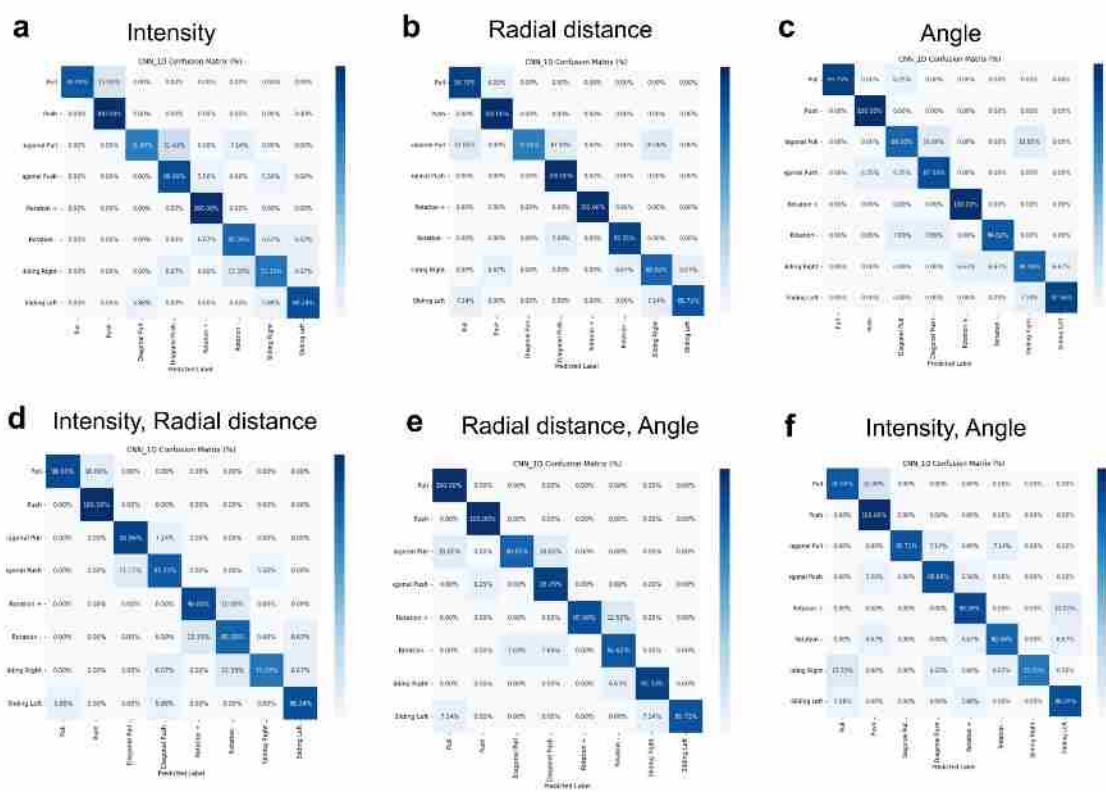
Figure S8. Confusion matrices comparing classification results with different feature data combinations as inputs to the CNN. a) Solely intensity, **b)** radial distance and **c)** angle of the centroid of the ML distribution. **d)** Combination of intensity and radial distance. **e)** Combination of radial distance and angle. **f)** Combination of intensity and angle.
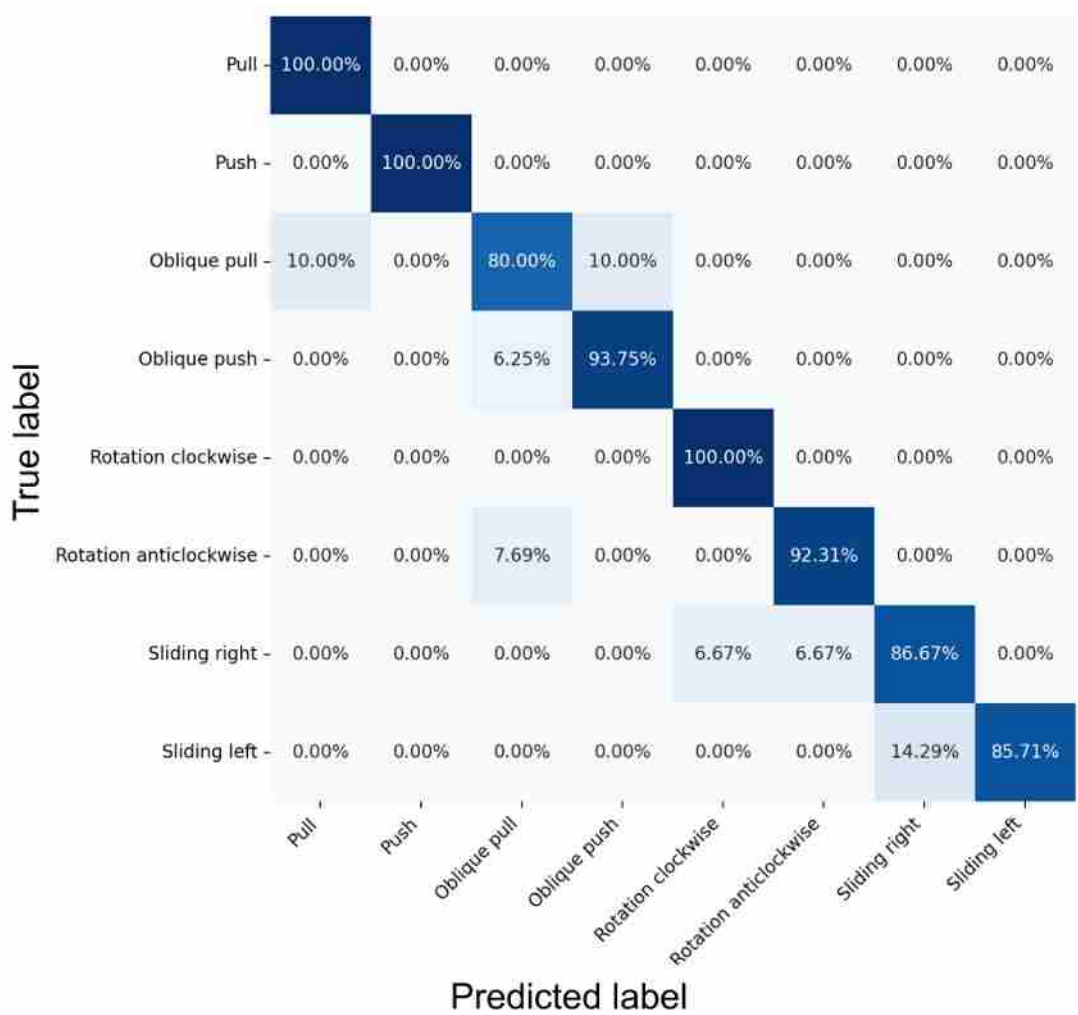
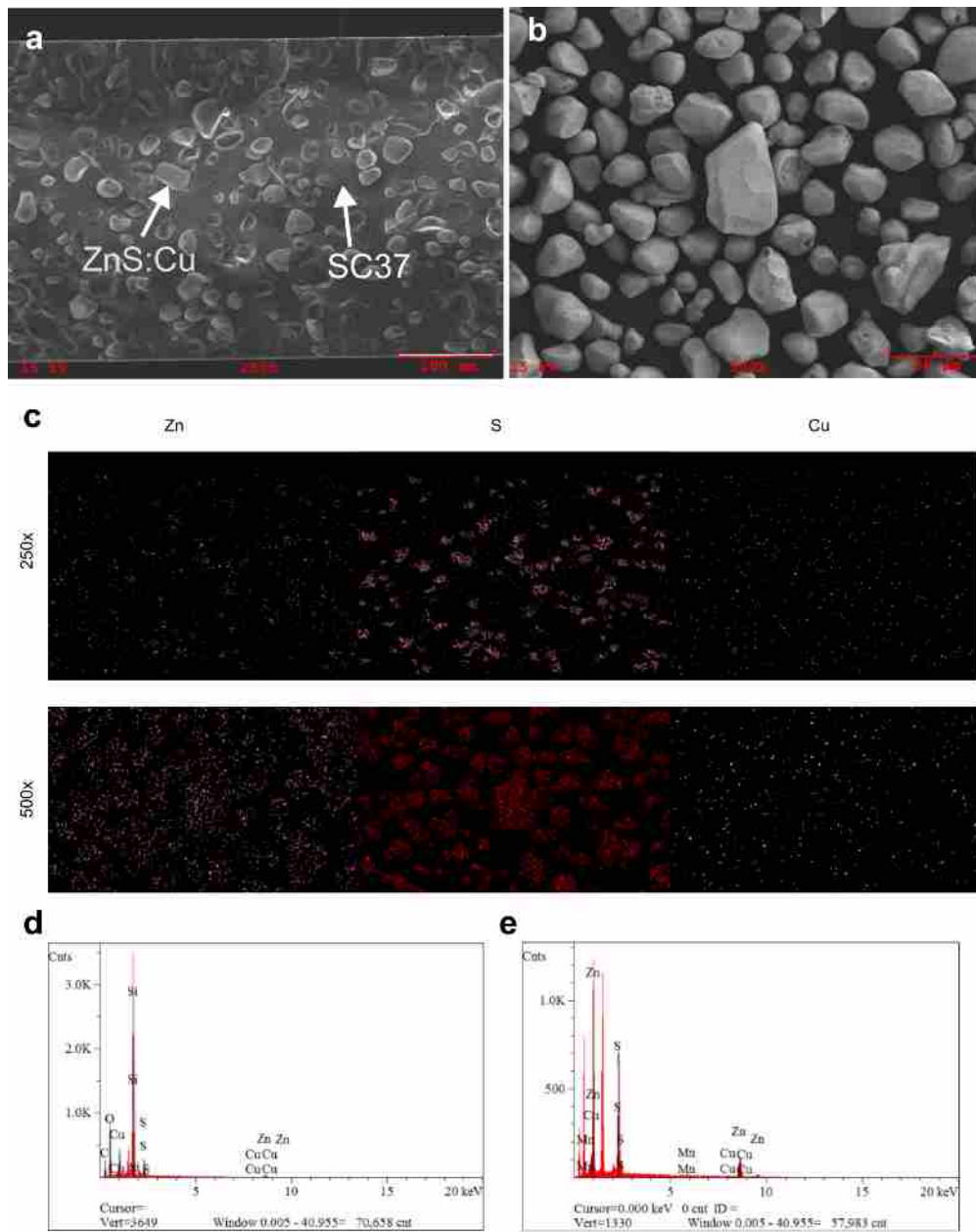**Figure S9. Confusion Matrix of the CNN model with 8 interaction types as inputs.**

Figure S10. Structural and elemental analysis of the ZnS:Cu and SC37 composite. a) Cross-sectional SEM image at 250x magnification showing the distribution of ZnS:Cu particles within the SC37. **b)** SEM image at 500x revealing the detailed morphology of ZnS:Cu particles. **c)** Elemental mapping at 250x and 500x magnifications for zinc (Zn), sulfur (S), and copper (Cu), illustrating the distribution of these elements within the composite. **d)** X-ray diffraction pattern of **a**. **e)** X-ray diffraction pattern of **b**.
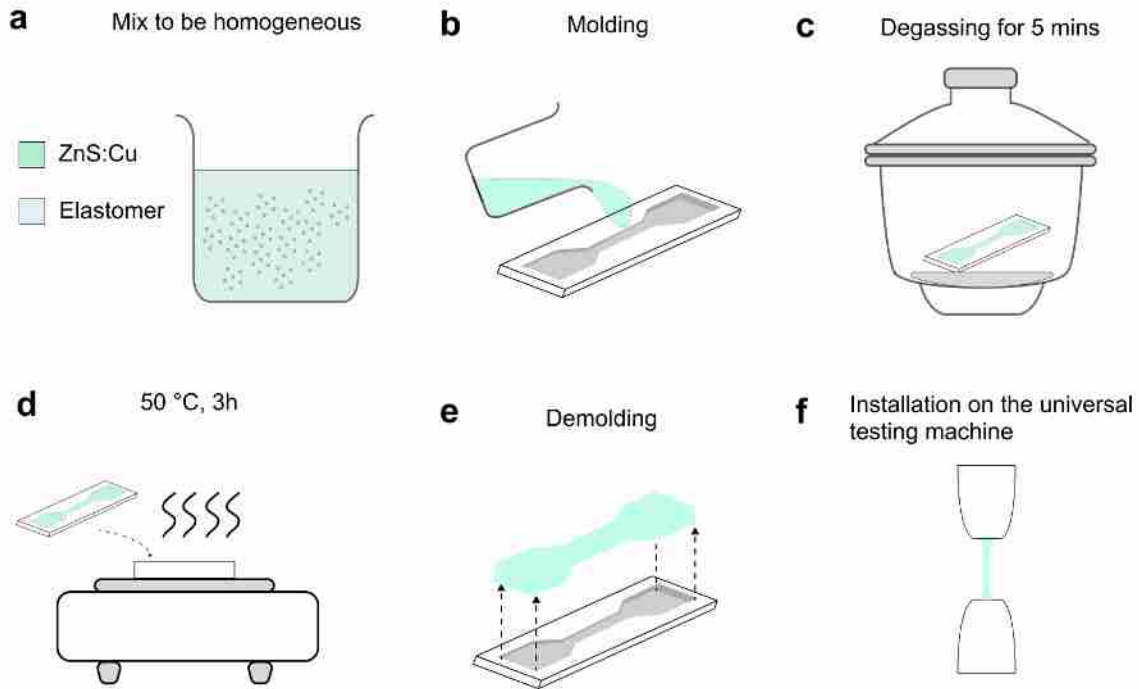
Figure S11. Fabrication process of the dog-bone shaped ML elastomers (ISO37 standard) for tensile tests. a) Add ZnS:Cu and elastomer into a container and mix it using a Planetary Centrifugal Mixer. **b)** Cast the ML elastomer onto the ISO37 mold. **c)** Vacuum the ML elastomer mold at 30 kPa to remove bubbles. **d)** Thermal curing at 60°C. **e)** Demold the ISO37 ML elastomer. **f)** Install ISO37 ML elastomer onto the universal machine.
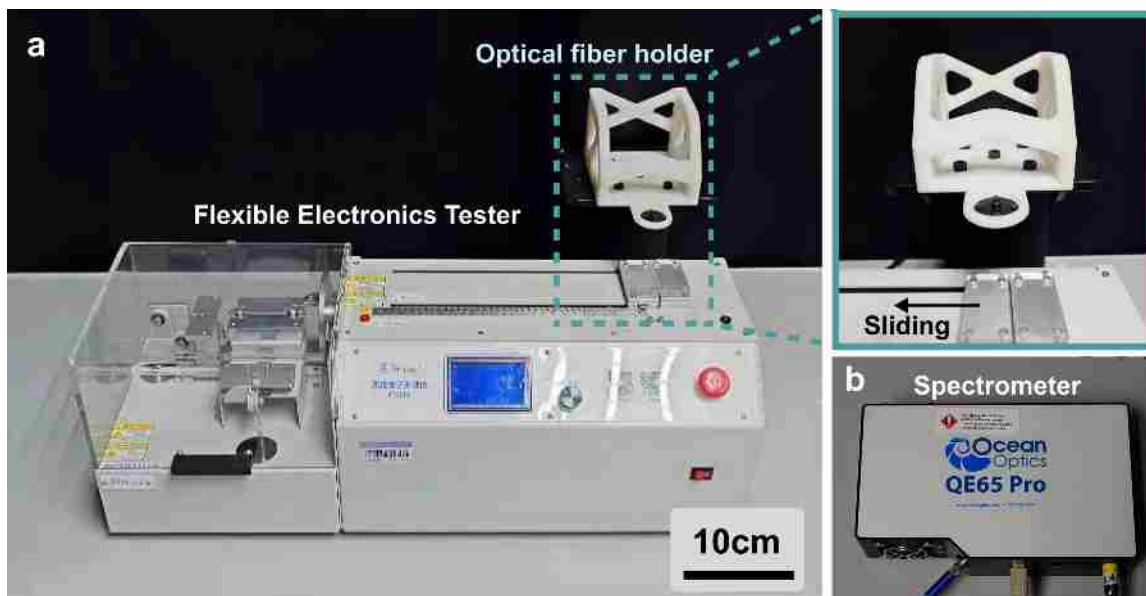
Figure S12. Experimental setup for evaluating the mechano-to-photon conversion efficiency of ML composite films. a) The setup includes a cupping machine for sample elongation and a lifts for connent the fibre from the spectrometer. **b)** An Ocean Optics QE65 Pro spectrometer is connected for measuring light emissions from the films upon deformation.
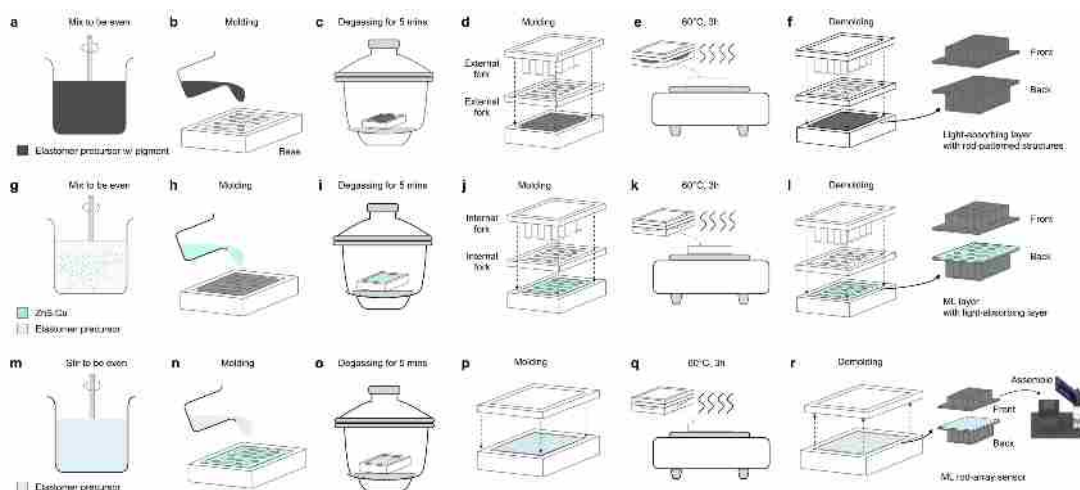
Figure S13. Fabrication process of the ML rod-array elastomer. a) Add rubbber and black pigment into a container and mix it using a Planetary Centrifugal Mixer. **b)** Cast the elastomer onto the patterned base mold. **c)** Vacuum the elastomer mold at 30 kPa to remove bubbles. **d)** Insert the fork and filter mold onto the elastomer. **e)** Thermal curing at 60°C. **f)** Demold the light-absorbing layer. **g-l)** Repeat the process for the ML layer. **m-r)** Repeat the process for the rubber core layer, following the same steps. Finally, assemble the ML rod-array sensor onto the sensing module.
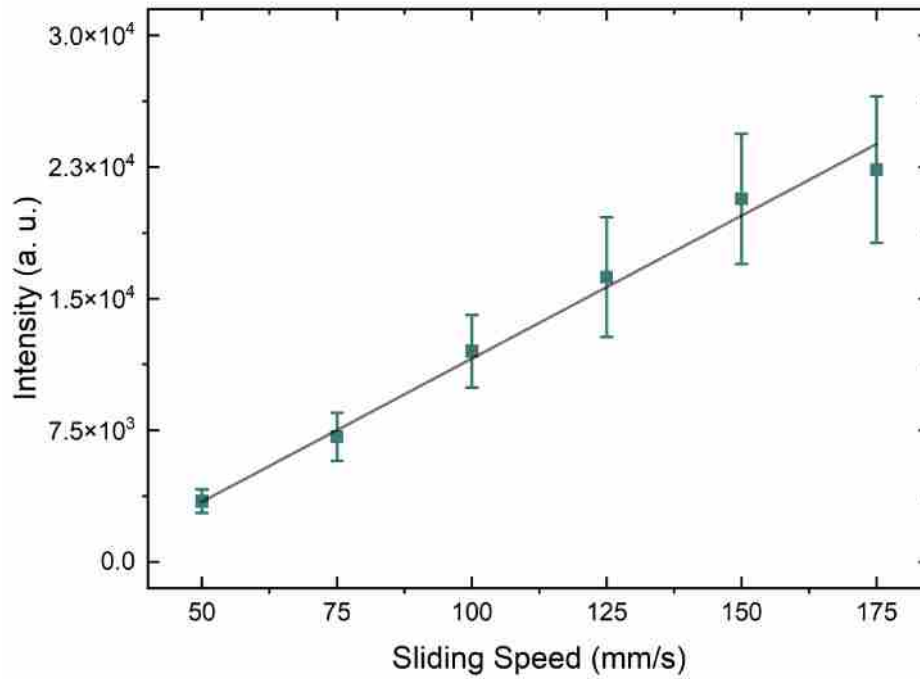
Figure S14. Speed-intensity correlation in ML elastomers: displays the relationship between sliding speed and ML emission intensity for a robotic finger sliding across an ML elastomer at six distinct velocities. The data shows a positive correlation between sliding speed and intensity, as evidenced by a high logarithmic regression coefficient (R^2 = 0.98).
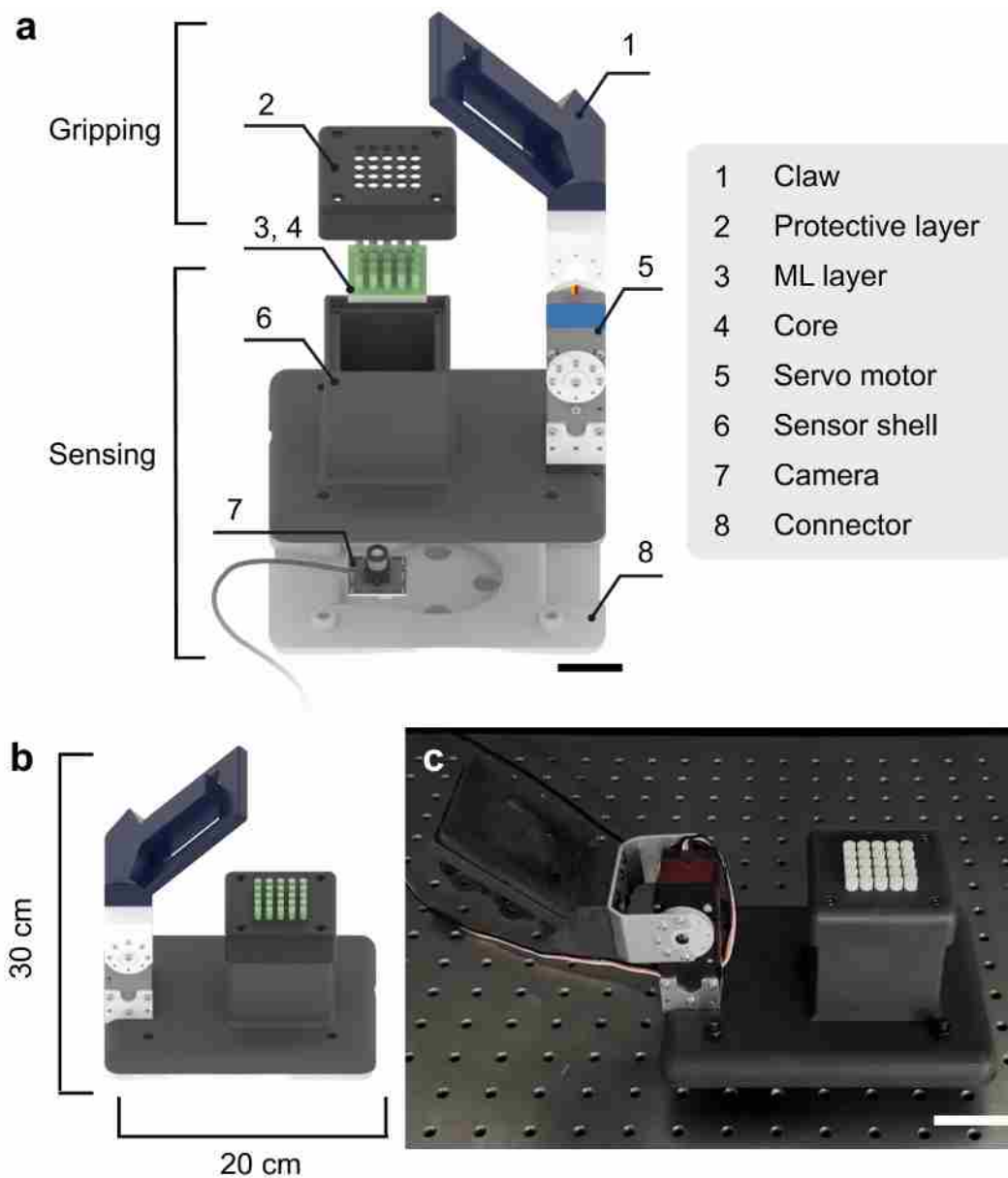
Figure S15. The schematic representation and photograph of the MAVIG. a) Exploded view of the MAVIG system. Scale bar, 3 cm. **b)** Dimensions of the gripping system. **c)** Photograph of the gripping system with the ML Elastomer (without the light-absorbing layer assembled). Scale bar, 4 cm.
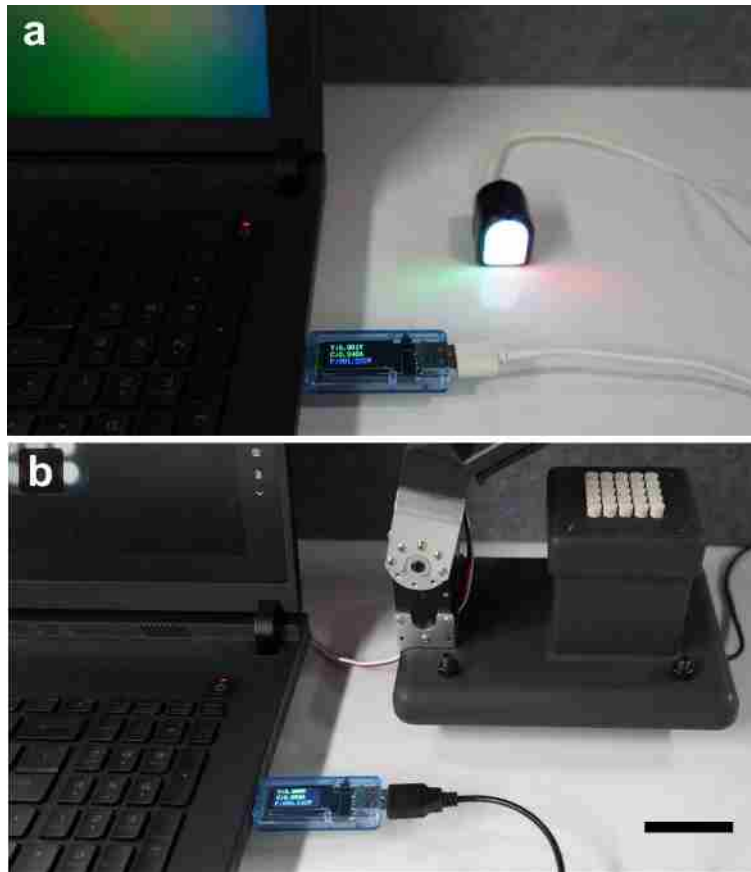
Figure S16. Experimental setup for evaluating the power consumption of different visuotactile sensors via a USB power-meter connected to a computer. The sensors were adjusted to their maximum resolutions during the experiment. a) The measurement of the commercial visuotactile sensor DIGIT's power consumption. **b**) The measurement of the ML-powered gripping system's sensing module. Scale bar, 4 cm.

Algorithm 1: Dynamic Luminescent Localization Mapper

```
/* Loading hardware calibration parameters */
// There are 25 distinct regions corresponding to the 25 rods.
```

Data: Centre coordinates $C = \{c_a(x,y)\}_{a=1,2,\ldots,25}$ and average radius $\overline{R}$ of each taxel

```
/* Initialization D = 0, {B_a = 0}_{a=1,2,...,25} */
// Read video frames at 30 FPS for 1 s
```

for $t \leftarrow 1$ **to** 30 **do**
    $D+ = \mathbf{M}(t)$ // The total brightness of each frame $\mathbf{M}(t)$
    for $a \leftarrow 1$ **to** 25 **do**
        $B_a+ = \mathbf{H}(t)$ // The total measurement of one of the circular areas $\mathbf{H}_a(t)$
    end
end
$D/= 30, \{B_a/= 30\}_{a=1,2,\ldots,25}$
while DLLM is active **do**
    $\{H_a = 0, l_a = 0, \omega_a = 0\}_{a=1,2,\ldots,25}$
    update $\mathbf{M}(t), \{\mathbf{H}_a(t)\}_{a=1,2,\ldots,25}$ from current frame $I(x,y)$
    `/* Global event-driven threshold α */`
    if $M(t) > \alpha D$ **then**
        for $a \leftarrow 1$ **to** 25 **do**
            `/* Local event-driven threshold β */`
            if $H_a(t) > \beta B_a$ **then**
                $l_a, \omega_a =$ FeatureExtraction$(I(x,y), \{c_a(x,y)\}_{a=1,2,\ldots,25}, \overline{R})$
            end
        end
    end
    `/* Store the data or send it to the next stage for processing */`
    CNN or Dataset $\Leftarrow Z_a(t) = (H_a, l_a, \omega_a)$
end
Function FeatureExtraction$(I(x,y), \{c_a(x,y)\}_{a=1,2,\ldots,25}, \overline{R})$:
    $\vec{v}_a(t) = q_a(t) - c_a$ // Weighted centroid coordinates $q_a(t)$
    $l_a(t) = \sqrt{v_{a,x}^2 + v_{a,y}^2}$
    $\omega_a(t) = arctan(\frac{v_{a,y}}{v_{a,x}})$
    return l_a, ω_a
End Function

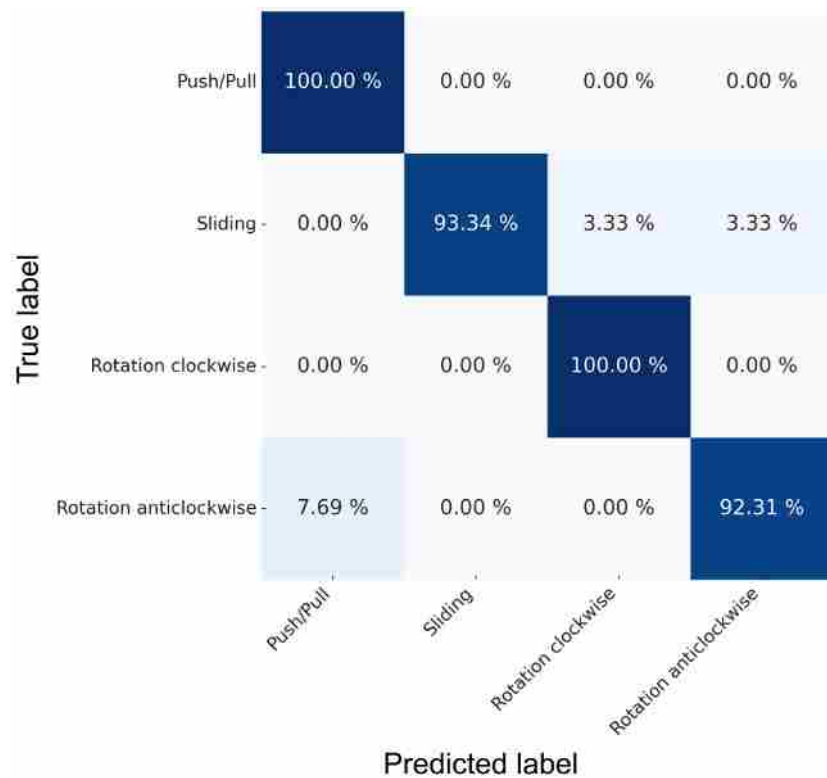**Figure S17. The pseudocode of DLLM and the process toward CNN network**

Figure S18. Confusion matrix of the classification performance across four motion types: Push/Pull, Sliding, Rotation clockwise, and Rotation anticlockwise.

Table S1. Characteristic comparison of reported sensors for mechanical stimuli

Sensor type	Distributed detection*	Material	Power consumption	Adaptability	Reference
Piezophotonic sensor	No	PET and ZnS:Mn	None	High	Nat. Photonics 7(9) (2013): 752. Adv. Mater., 2015, 27(14)
Piezoelectricity sensor	No	PDMS, polyester and stainless steel	None	Low	Nat. Electron. 571, 578 (2020)
Optical lace structure	Yes	Polyurethane	High	Low	Sci. Robot. 4, eaaw6304 (2019)
Stretchable distributed fiber	Yes	Silica gel and dye	High	High	Science 370, 848 (2020)
Mechanoluminescent optical fiber sensor	Yes	PDMS and doped ZnS	None	Low (Dark condition)	Nat. Electron. 682, 693 (2022)
Mechanoluminescent visuotactile sensor	Yes	SC37 and ZnS:Cu	None	High (Environmental versatility)	This work

*Distributed detection refers to a method that identifies changes in mechanical stimuli at various positions by analyzing the optical signal at the end.

Table S2. Systematic comparison of conventional and ML-based sensing architectures

Characteristics	Piezoresistive	Capacitive	Optical waveguide	Traditional visuotactile (e.g., GelSight)	ML-based visuotactile (This work)
Adaptability	Fixed calibration required	Environmental interference sensitive	Limited by waveguide design	Fixed calibration needed	Self-recoverable operation
Data processing	Continuous sampling	Continuous sampling	Continuous optical readout	High-resolution continuous imaging (11.025M pixels/s)	Event-driven
Power requirements	Low (0.1-0.5 W)	Medium (0.3-0.8 W)	High (>1 W)	High (1.222 W, LED system)	Medium (0.542 W)
System complexity	Multiple wiring points	Complex electrode patterns	Optical coupling required	LED array + camera system	Single USB connection
Environmental stability	Temperature sensitive	Humidity sensitive	Light interference	Thermal degradation in LEDs	Stable under varied conditions

Reference

[S1] M. S. Lopes, A. P. Moreira, M. F. Silva, F. Santos, in *EPIA Conference on Artificial Intelligence*, Springer, 2023.

[S2] S. Zimmermann, R. Poranne, S. Coros, in 2021 International Conference on Robotics and Automation (ICRA), 2021.

[S3] a) C. D. Bellicoso, K. Krämer, M. Stäuble, D. Sako, F. Jenelten, M. Bjelonic, M. Hutter, in *2019 International Conference on Robotics and Automation (ICRA)*, IEEE, 2019; b) J.-P. Sleiman, F. Farshidian, M. V. Minniti, M. Hutter, *IEEE Robotics and Automation Letters* **2021**, 6, 4688.

[S4] a) Y. Hu, B. Chen, J. Lin, Y. Wang, Y. Wang, C. Mehlman, H. Lipson, *Science Robotics* **2024**, 9, eadi4724; b) F. Krueger, K. C. Mitchell, G. Deshpande, J. S. Katz, *Animal Cognition* **2021**, 24, 371.